





# Giant nonlinear Hall effect in twisted WSe<sub>2</sub>

Meizhen Huang<sup>1,2</sup>, Zefei Wu<sup>1,2</sup> , Jinxin Hu<sup>1,2</sup>, Xiangbin Cai<sup>1</sup>, En Li<sup>1</sup>, Liheng An<sup>1</sup>, Xuemeng Feng<sup>1</sup>, Ziqing Ye<sup>1</sup>, Nian Lin<sup>1</sup>, Kam Tuen Law<sup>1</sup> , Ning Wang<sup>1</sup> 

<sup>1</sup>Department of Physics and Center for Quantum Materials, The Hong Kong University of Science and Technology, Hong Kong, China

<sup>2</sup>These authors contributed equally: Meizhen Huang, Zefei Wu, Jinxin Hu.

 e-mail: phwang@ust.hk; phlaw@ust.hk; wzefei@connect.ust.hk

## Abstract

**A finite Berry curvature dipole can induce a nonlinear Hall effect in which a charge current induces a second harmonic transverse electric voltage under time-reversal-symmetric condition. Here, we report the transport measurement of giant nonlinear Hall effect in twisted WSe<sub>2</sub> homobilayers as evidenced by the dominated second harmonic Hall voltage that scales quadratically with the injection current. Benefited from strain-induced symmetry breaking, the nonlinear Hall effects are measurable globally along all in-plane directions. At the half-filling of the hole moiré superlattice band in twisted WSe<sub>2</sub> where interaction effects are strong, we observe a record high nonlinear Hall responsivity of  $10^{10}$  VW<sup>-1</sup>. Our work demonstrates a new and highly tunable correlated system to achieve nonlinear Hall effect and provides potential device applications using artificially constructed van der Waals superlattices.**

The Berry curvature (BC) in momentum space can give rise to novel transport phenomena in materials with broken time-reversal or inversion symmetry<sup>1, 2, 3</sup>. The non-trivial BC plays a key role in quantum Hall effects in two-dimensional electron gas systems under external magnetic fields<sup>1</sup>, anomalous Hall effects in magnetic materials<sup>2, 4</sup>, and valley Hall effects in inversion asymmetric materials<sup>5, 6</sup>. While the zeroth-order moment of the BC is related to the Hall responses at the same frequency as the input, theoretical calculations pointed out that the first-order moment of the BC, the so-called Berry curvature dipole (BCD)  $\mathbf{D}$ , can result in both DC and second harmonic Hall responses (Fig. 1a), namely, the nonlinear Hall effect<sup>7, 8, 9</sup>. Two-dimensional device structures based on the nonlinear Hall effect have potential applications in high-frequency and high-efficiency second harmonic generation and rectification. The frequency doubling and rectification through the nonlinear Hall effect are achieved by the intrinsic material property, offering a highly sensitive approach for ultra-low signal processing operational at cryogenic temperatures. This kind of device structure does not have any thermal voltage threshold and/or the transition time innate to semiconductor junctions/diodes<sup>10, 11</sup>.

Theoretically, the non-vanishing BC is accompanied by the breaking of the time-reversal or the inversion symmetry, whereas the emergence of the BCD requires extra crystalline symmetry breaking<sup>12, 13, 14, 15, 16, 17, 18</sup>. Till now, experimental observations of the nonlinear Hall effect have only been achieved in either pristine WTe<sub>2</sub> (ref. 19, 20) or strained MoS<sub>2</sub> (ref. 21) and graphene<sup>22</sup>, in which the nonlinear Hall signals can only survive when the in-plane input is not parallel to the crystal's mirror plane or not perpendicular to the exerted strain.

Moiré superstructures generated by stacking the same material with a small rotation angle or by stacking two materials with similar lattice constants can largely modulate the band structures and transport properties of these materials<sup>23, 24, 25, 26, 27</sup>. Unconventional phenomena such as

superconductivity<sup>28, 29, 30, 31, 32</sup> and Mott-like insulating phases<sup>33, 34, 35, 36, 37</sup> have been observed in twisted graphene and twisted transition-metal dichalcogenides (TMDCs). Compared with twisted graphene, the symmetries in twisted TMDCs are more complicated since one monolayer TMDC consists of one layer of transition metal atoms and two layers of chalcogen atoms. Experimentally, rotational and mirror symmetry breaking in twisted WSe<sub>2</sub> (tWSe<sub>2</sub>) from either spontaneous or substrate/interface effects have been observed by scanning tunneling microscopy (STM) topography<sup>38</sup>. The intrinsically broken inversion symmetry causes the emergence of BC hotspots, while the three-fold asymmetry creates BCDs (Fig. 1b, c). Along with the small gap of spin-split moiré bands which enhances the BC amplitude, twisted TMDCs become a potential platform for observing nonlinear Hall effects. Using the artificial construction of van der Waals moiré superlattices to break symmetries opens a new way to generate and probe the BCD properties in materials.

In this work, we report the first transport measurement of nonlinear Hall effects in tWSe<sub>2</sub> moiré superlattices whose broken symmetries are verified by scanning transmission electron microscopy (STEM) and STM characterizations. Upon applying an in-plane AC electric field, a prominent second harmonic Hall voltage that scales quadratically with the injected current is detected. Gate-, temperature- and angular-dependent nonlinear Hall effects are investigated in different samples. Unlike the situation in naturally-formed crystalline materials<sup>19, 20, 21</sup>, the nonlinear Hall signals in artificially constructed tWSe<sub>2</sub> are measurable globally at any in-plane directions. Very strikingly, the measured nonlinear Hall responsivity near the half-filling of the tWSe<sub>2</sub> moiré unit cell reaches  $10^{10} \text{ VW}^{-1}$  at  $T = 1.5 \text{ K}$ , which is six orders of magnitude higher than the maximum responsivity reported so far<sup>19, 39</sup>. Away from half-filling, the general theory (no interaction effects) proposed by Sodemann and Fu<sup>7</sup> gives qualitative understand of the data. However, near half-filling, interaction

effects are indeed rather important, we discuss and interpret the giant nonlinear Hall responsivity by considering interaction-induced gapped phases.

Twisted WSe<sub>2</sub> structures were fabricated using the “tear-and-stack” method<sup>28, 29, 40</sup> (see details in Methods). Fig. 1d shows two typical features of tWSe<sub>2</sub> samples as observed by STEM. Firstly, the twist angle ( $\sim 1.8^\circ$ ) can be determined by measuring the moiré lattice scale and the angular difference between the two sets of electron diffraction patterns shown in the inset. Secondly, the moiré superlattice exhibits strong distortion as outlined by the red dashed lines connecting the nearest AA stacking points. The moiré unit cells joint at these AA points with angles of  $77^\circ$ ,  $54^\circ$  and  $49^\circ$ , largely deviating from the ideal angle of  $60^\circ$ . Using a uniaxial heterostrain model and the distance between three nearest AA points in each triangle, we estimate the maximum lattice strain  $\varepsilon = 1.13\%$ , the minimum strain  $\varepsilon = 0.65\%$  and the average uniaxial strain  $\varepsilon = 0.90\%$  (see Supplementary Section I)<sup>41</sup>. Note that the calculated strain is averaged over a small triangle, the local strain at individual atom bonds can be larger or smaller than the average strain. The inhomogeneous contrast inside each triangle clearly reveals the lattice symmetry breaking and inhomogeneous strain occurring inside the superlattice. As illustrated by a STM image shown in Fig. 1e, similar deformation effects occur in the sample and the moiré unit cells are hardly hexagonal. The enlarged image of the area marked by the dark square is a scalene hexagon. The local twist angle ( $\sim 2.1^\circ$ ) and strain strength ( $\varepsilon = 0.6\%$ ) can be extracted using the same uniaxial heterostrain model (see Supplementary Section I).

On the base of STEM and STM characterization for tWSe<sub>2</sub> samples with twist angles ranging from  $1^\circ$  to  $4^\circ$ , we conclude that significant symmetry breaking effects mainly caused by the substrate effects and twist angle variation from the construction of the device structures during the fabrication process<sup>42, 43</sup> universally exist in tWSe<sub>2</sub>. In principle, the broken rotational and mirror

symmetries would segregate the BC with different signs and result in a Berry curvature dipole strength  $\mathbf{D}$  near the Fermi level as discussed later in theoretical calculations. As a result, a nonlinear Hall current  $J_{NLH}$  with frequency  $2\omega$  should be generated if an external electric field with frequency  $\omega$  is applied parallel to  $\mathbf{D}$  (Fig. 1a).

In this work, twisted double-monolayer/-bilayer/-trilayer p-type (hole carriers) WSe<sub>2</sub> (labeled as sample A/B/C, respectively) devices were fabricated and systematically studied. Fig. 1g shows the transport characteristics of a typical high-quality tWSe<sub>2</sub> device (sample B with a twist angle  $\theta = 3.1 \pm 0.2^\circ$ , see Supplementary Section II for the determination of  $\theta$ ) built with a top-gate electrode (Fig. 1f), in which the resistance  $R$  is plotted as a function of the carrier density  $n$  at the temperature  $T = 1.5$  K. The full filling of a moiré unit cell can be estimated based on  $n_0 = 2/\left(\frac{\sqrt{3}}{2}\lambda^2\right) = 6.15 \times 10^{12} \text{ cm}^{-2}$ , where  $\lambda = a/(2 \sin \frac{\theta}{2})$  is the moiré superlattice constant calibrated using the lattice constant of WSe<sub>2</sub>  $a = 0.329$  nm and the twist angle  $\theta = 3.1 \pm 0.2^\circ$ . The appearance of a resistance peak at gate voltage  $V_{tg} = -9.2$  V (corresponding to half-filling, i.e., the top valence band is half-filled at  $n = n_0/2 = 3.08 \times 10^{12} \text{ cm}^{-2}$ ) indicates the existence of strong correlation effects within the first moiré band. The dramatic drops of the resistance to zero at  $V_{tg} = -9.5$  V and  $V_{tg} = -8.8$  V can be attributed to the correlated metallic states adjacent to half-filling<sup>28, 31</sup>. We also measured the  $T$ -dependent resistances and superconducting signatures (See Supplementary Section III), which are consistent with the results reported from other high-quality twisted devices<sup>28, 29, 31, 33</sup>.

To measure the nonlinear Hall effects in the tWSe<sub>2</sub>, an AC bias voltage at a fixed frequency ( $\omega = 4.579$  Hz) is applied. The induced current ( $I$ ) at the same frequency and voltage drops along the longitudinal ( $V_{//}$ ) and transverse ( $V_{\perp}$ ) directions at the second harmonic  $2\omega$  frequencies are

recorded. The responses of the second harmonic Hall voltage  $V_{\perp}^{2\omega}$  to the injection current  $I$  for samples A, B and C are shown in Fig. 2a. Three obvious features are observed. Firstly,  $V_{\perp}^{2\omega}$  increases nonlinearly and scales quadratically with  $I$  for all three samples. Secondly,  $V_{\perp}^{2\omega}$  changes its signs when both the voltage detection and current injection directions are reversed. Thirdly, sample A (1L+1L)/sample B (2L+2L) produces the highest/lowest  $V_{\perp}^{2\omega}$  signal, respectively. To illustrate the details of the property changes of the nonlinear Hall effect, we first mainly show the representative data from sample B in Fig. 2b-g. The behaviour of all three samples are similar, and additional nonlinear transport data can be found in Supplementary Section IV.

Fig. 2b demonstrates the typical data of  $V_{\perp}^{2\omega}$  versus  $I^2$  taken from sample B. We find that  $V_{\perp}^{2\omega}$  (red dots) vanishes, while  $V_{\perp}^{2\omega}$  measured using various electrode configurations changes linearly with  $I^2$  (black dots and blue dots). Such a Hall dominated second harmonic signal can exclude other possible effects such as the contact junction, flake shape, and thermoelectric effects induced second harmonic generation, and verifies the BCD induced nonlinear Hall effect in tWSe<sub>2</sub><sup>19</sup>. Different from previously reported data in WTe<sub>2</sub> and strained MoS<sub>2</sub>, when we exchange the current injection with the Hall voltage measurement directions, we still get a non-vanishing second harmonic Hall voltage (green dots in Fig. 2b)<sup>19, 20, 21</sup>. Since the crystal edge is not aligned to the electrodes in sample B, whether such a non-vanishing Hall voltage reveals mirror symmetry breaking is not clear and will be discussed later. Additional transport data such as DC response and frequency dependence of the nonlinear Hall signal is shown in Supplementary Section IV.

Next, we investigate the second harmonic Hall response  $V_{\perp}^{2\omega}$  as a function of  $n$ , or equivalently  $V_{\text{tg}}$  in the measurement, at a fixed longitudinal current  $I = 20$  nA. As shown in Fig. 2c,  $V_{\perp}^{2\omega}$  experiences a sharp increase after the channel is switched on at  $V_{\text{tg}} = -5.8$  V. Then, it fluctuates

and tends to decrease with increasing  $n$ . It remains non-zero in the whole range where we measured the sample. The  $V_{\perp}^{2\omega} - I^2$  relationship at different  $V_{\text{tg}}$  is shown in Fig. 2d. In the whole range of  $V_{\text{tg}}$  we measured,  $V_{\perp}^{2\omega}$  increases nonlinearly and scale quadratically with  $I$ . Therefore, the nonlinear Hall effect is robust at all gate voltages.

We then further investigate the temperature dependent nonlinear Hall effect. From Fig. 2e, we can see that  $V_{\perp}^{2\omega}$  scales quadratically with  $I$  at different temperatures, and that the nonlinear Hall signals become lowered at higher  $T$ . Quantitatively, the strength of the nonlinear Hall signal can be evaluated through  $V_{\perp}^{2\omega}/(V_{\parallel})^2$  (the higher value, the higher nonlinear response), where  $V_{\parallel}$  depends linearly with  $I$  according to the Ohm's law. As plotted in Fig. 2f, the fitted  $V_{\perp}^{2\omega}/(V_{\parallel})^2$  decreases monotonically with increasing temperature and reduces to nearly zero at  $T = 30$  K. The upturn trend of the longitudinal conductivity  $\sigma_{xx}$  versus  $T$  indicates insulating behaviour at the gating condition we used. Both  $n$  and  $T$  dependences demonstrate a higher nonlinear Hall signal at a lower  $\sigma_{xx}$ , which is in accordance with the BCD induced effect but inconsistent with the disorder induced effect<sup>19</sup>. Meanwhile, it should be noted that though the BCD dominates in our sample, the linear fitting in Fig. 2g cannot rule out the possibility from other second harmonic transport mechanisms (see Supplementary Section V for more details)<sup>45</sup>.

According to previous reports<sup>7, 9, 15</sup>, the BCD induced nonlinear Hall current can be expressed as:  $\mathbf{J}^{2\omega} = \frac{e^3\tau}{2\hbar^2(1+i\omega\tau)}(\hat{\mathbf{c}} \times \mathbf{E}^{\omega})(\mathbf{D} \cdot \mathbf{E}^{\omega})$ , where  $\hbar$  is the reduced Planck constant,  $e$  the elementary charge and  $\tau$  the relaxation time. It means that the nonlinear Hall signal is normal to the source  $\mathbf{E}$  and nonparallel to  $\mathbf{D}$ . As  $\mathbf{D}$  is perpendicular to the sample mirror plane (if a mirror exists), in order to verify the breaking of mirror symmetry, we fabricate disc-shaped devices and examine the angular dependence of the nonlinear Hall effect. If any mirror symmetry along certain in-plane

direction is preserved,  $V_{\perp}^{2\omega}$  must be zero when the external electric field is applied along the mirror plane ( $\mathbf{D} \cdot \mathbf{E}^{\omega} = 0$ )<sup>7, 19, 20, 21</sup>. Fig. 3a reveals the optical image of sample A (twist angle  $2.0 \pm 0.2^{\circ}$ ) constructed with twelve bottom electrodes in circular distribution. The naturally cleaved edge (armchair or zigzag) of WSe<sub>2</sub> is aligned with one pair of the electrodes along the diameter of the circular device which are set to be  $\theta = 0^{\circ}$  and  $\theta = 180^{\circ}$ . Therefore  $\theta = 90^{\circ}$  and  $\theta = 270^{\circ}$  is the other cleaved edge. The angular dependent  $V_{\perp}^{2\omega}$  is measured in a clockwise sequence and shown in Fig. 3b. Similar to the devices of bulk WTe<sub>2</sub>, the measured  $V_{\perp}^{2\omega}$  from our samples also changes signs at different  $n$ . However, the values of  $V_{\perp}^{2\omega}$  are nonzero along all directions in our samples (see more in Supplementary Section VI), while in WTe<sub>2</sub> or strained MoS<sub>2</sub>,  $V_{\perp}^{2\omega}$  is zero along the mirror plane<sup>19, 20, 21</sup>. The observed global nonlinear signals evidence that there is no mirror symmetry in our sample, consistent with the STEM and STM results. One more apparent feature is that the values of  $V_{\perp}^{2\omega}$  along different directions vary largely, ranging from 0.01 mV to 10 mV, which implies that the strain is highly inhomogeneous in the sample. This inhomogeneity has also been confirmed by our STEM and STM studies (See Supplementary Section I). We find that the nonlinear Hall signal strengths measured from different regions in the sample often vary largely (See Supplementary Fig. 11) and realize that the mesoscopic nonlinear signal we measured is actually an average result of the microscopic responses in the sample.

Since the nonlinear Hall effect is induced by the non-zero  $D$ , we adopt the formula  $D = \frac{2\hbar^2(\sigma_{xx})^3 V_{\perp}^{2\omega} W}{e^3 \tau I^2}$  to estimate the BCD strength<sup>7</sup>, where  $W$  is the sample width and  $\tau = \frac{\sigma_{xx} m^*}{ne^2}$  is the relaxation time (See Methods for details). However, unlike most material systems where the effective mass  $m^*$  can be obtained from non-interacting first-principle calculation, the effective mass of hole carriers in twisted WSe<sub>2</sub> is still an unknown parameter because of the complexity of the flat moiré bands and strong electron-electron interactions in such a system. There is no direct



way to measure  $D$ , but we can obtain the value of  $Dm^*$  (see Supplementary Section VII for  $Dm^*$  in different samples). To evaluate the transfer efficiency of the nonlinear signal, the responsivity  $\gamma = \frac{V_{\perp}^{2\omega}}{I^2 R}$  (defined as the ratio between the nonlinear Hall voltage and the applied source power which can be directly measured) is calculated and shown in Fig. 3c. The highly anisotropic value of  $\gamma$  displays similar features with the absolute value of  $V_{\perp}^{2\omega}$ . Just like the spin Hall angle that measures the spin current generation efficiency, the larger  $\gamma$ , the larger  $2\omega$  and DC signals. As shown in Fig. 3d in which  $Dm^*/m_e$  and responsivity  $\gamma$  in sample A (along  $\theta = 0^\circ$ ) is plotted, the responsivity has an average value around  $10^7 \text{ VW}^{-1}$ , which is three orders of magnitude larger than that in previous studied materials<sup>19, 39</sup>. At the half-filling of the moiré unit cell, the responsivity further increases and reaches as high as  $10^{10} \text{ VW}^{-1}$  (See Supplementary Section VII). Such a large value highlights the great potential of using artificially constructed twist structures of van der Waals materials for nonlinear signal generations.

Similar results are obtained from sample C (twist angle  $2.0 \pm 0.2^\circ$ ) as shown in Fig. 3f and 3g. Compared with sample A (Fig. 3d), sample C (Fig. 3h) has a relatively large value of  $Dm^*$  and a small value of  $\gamma$ . This difference could be explained as follows. In sample C,  $\Gamma$  and Q valleys may contribute to the transport, and more bands are folded into the moiré Brillouin zone. The narrowed band gap and the enhanced density of states should increase the BCD (see Fig. 3e) since BC is inversely proportional to the gap size. However, the responsivity (characterized by  $\gamma \propto \frac{Dm^* R}{n}$ ) depends not only on  $D$  but also on the effective mass and the sample resistance. The enhanced dipole and decreased resistance compete with each other, making the responsivity in sample C a bit smaller than that in sample A. We also list the values of  $Dm^*$  and  $\gamma$  for all three samples in Supplementary Table 7, in which sample B has lowest values of  $Dm^*$  and  $\gamma$ . This can

be attributed to the presence of inversion symmetry in pristine bilayer WSe<sub>2</sub> in this sample (detailed analysis can be found in Supplementary Section VII), considering a similar level of strain-induced symmetry breaking effects in all three samples.

To understand the origin of the giant nonlinear Hall signal, we perform calculations using a continuum model (see Supplementary VIII and ref. 46). As an example, the band structures, density of states, and Berry curvatures of 2° tWSe<sub>2</sub> are shown in Fig. 4. The BC for unstrained tWSe<sub>2</sub> is shown in Fig. 4d. In this case, the BCD, which measures the gain in total BC flux, must vanish<sup>14, 19</sup>. As mapped in Fig. 4e and 4f, the BCD cancels along zigzag ( $k_x$ ) and armchair ( $k_y$ ) directions. Fig. 4g depicts the calculated BC in tWSe<sub>2</sub> with uniaxial strain  $\varepsilon = 0.6\%$  along the zigzag direction. The unbalanced BCD distribution in Fig. 4g is displayed in Fig. 4h/4i along  $k_x/k_y$  direction, respectively. The breaking of three-fold rotational symmetry results in finite BCD. Although the uniaxial strain model cannot fully simulate the real strain situation in the samples, this simulation demonstrates the importance of the strain to generate a non-zero  $D$ .

We consider that BCD, effective mass and sample resistance are three critical factors for producing the giant responsivity in twisted WSe<sub>2</sub>. Fig. 4j and 4k illustrate the simulation results of the BCD plotted as a function of filling factors. The simulated  $D$  is in the order of 1~10 nm, which is comparable to the values published in previous reports. Besides that, due to the presence of the flat band, the effective mass of hole carriers can be largely increased. For example, in twisted bilayer graphene, the effective mass near the charge neutrality point is about 25 times larger than that in monolayer graphene<sup>47</sup>. Considering a similar effect of effective mass renormalization in our samples, the effective mass in twisted WSe<sub>2</sub> can be 1 to 2 orders of magnitude larger than that in monolayer WSe<sub>2</sub> (a discussion can be found in Supplementary Section IX). Therefore, away from

half-filling, the sizeable dipole and the large effective mass can explain the large responsivity of the samples qualitatively.

At half-filling, however, the strong enhancement of the responsivity shown in Fig.3d cannot be understood from the non-interacting electron picture. At half-filling, resistance peaks emerge as shown in Supplementary Fig.4 for all the three samples. Furthermore, the resistance at half-filling increases as temperature decreases (as shown in Supplementary Fig.7). This is a strong indication that an insulating correlated phase appears near half-filling. To explain the observed increase in resistance peak, we note that interaction effect can drive the system to an insulating correlated state such as the inter-valley coherent (IVC) state<sup>48</sup>. We performed a self-consistent mean-field calculation for the IVC order parameter including the interaction effects and the details can be found in Supplementary X. The finite IVC order parameter generates an insulating gap at half-filling. It is important to note that for a non-uniform sample, we expect that it is difficult to tune the whole sample to half-filling at the same time and there is always charge carriers even at half-filling. Moreover, we calculated the BC and the BCD of the IVC phase using the reconstructed band structure and found sizable BCD (See Supplementary Section X for the details). The enhancement of the resistance near half-filling together with the sizable BCD and effective mass enhancement can provide a possible explanation of the giant enhancement of the nonlinear Hall responsivity. This is because the responsivity can be expressed as  $\gamma \propto \frac{Dm^*R}{n}$ . First, the density of states near half-filling is strongly depleted by interaction, resulting in an insulating behaviour and thus generating a large  $R$  value. Second, interaction effects can induce a metal to correlated insulator transition, making the effective mass divergent at half-filling (see Supplementary Section IX)<sup>49, 50</sup>. These should largely elevate the responsivity. By the way, it is important to note that the IVC phase studied here is one of the possible phases which can explain the insulating behavior

and provide a sizable BCD. To fully understand the physics of the correlated phase near half-filling, further theoretical and experimental studies are needed.

In summary, twisted TMDCs FET devices provide a new platform for introducing and manipulating giant nonlinear Hall effects in the absence of a magnetic field for the following reasons. First, twisted TMDCs possess larger BCs than that in pristine TMDCs due to the flat bands characteristics (see Supplementary XI). Second, lattice strain inevitably exists in twisted samples and breaks both the three-fold rotational symmetry and mirror symmetry. The broken symmetries transfer the BC hotspot to BCD moment and make the nonlinear Hall effect measurable along all in-plane directions (See Supplementary Section XII for the analysis of the origin of symmetry breaking). Third, besides the strain-induced symmetry breaking, we also highlight the role of the displacement electric field (generated by the applied  $V_{tg}$ , see Supplementary XIII), which energetically separates the sub-bands and BCs in the two moiré valleys (See Supplementary XIV) and makes the value of BCD away from the half-filling ( $\sim 3$  nm) the same order as the highest of all materials ever explored<sup>19, 39</sup>. Finally, the gapped phase induced by strong electron-electron interaction near half-filling can induce additional enhancement on the giant responsivity and generate a record high responsivity of  $10^{10}$  VW<sup>-1</sup>. This could provide opportunities for potential technological applications and guide future experiments in artificially twisted TMDCs, including the study of the interplay between topological properties and correlation effects in twisted structures with twist-angle-tunable interaction strength, such as the one that predicts topological phase transitions at full-filling of a moiré unit cell<sup>46</sup>.

## **Methods**

### **Device fabrication**

WSe<sub>2</sub> bulk crystals and the BN sources are bought from HQ graphene. For the transport devices, BN about 30 nm thick are exfoliated onto SiO<sub>2</sub>/Si substrates, and then 10 nm Pt electrodes are patterned on the BN using e-beam lithography (EBL), reactive ion etching and e-beam evaporation. Using polycarbonate/polydimethylsiloxane (PC/PDMS) on a glass slide, BN about 15-30 nm is picked up from the SiO<sub>2</sub>/Si substrate. Then, tWSe<sub>2</sub> is fabricated by the “tear and stack” method and transferred onto the prepatterned Pt electrodes<sup>40</sup>. Top gate is then patterned by a second-round EBL and e-beam evaporation. For STM investigation, samples are fabricated by transferring the stacked tWSe<sub>2</sub> onto the flat surfaces of graphite substrates for direct imaging.

### **Transport measurement**

Transport measurements were performed in cryogenic system which provides stable temperatures ranging from 1.4 to 300 K and fields up to 14 Tesla. The DC top gate was applied through our home-made DAC with resolution of 1 mV. AC bias voltage was applied to the source probe through SRS DS360. First and second harmonic signals were measured by Signal Recovery 7280 lock-in amplifier (impedance 100 M $\Omega$ ). The *I-V* curves were measured by Keithley 6430. The *dI/dV* curves were measured by SRS DS360 and SRS 830.

### **STM measurement**

STM investigations were carried out at 77K in an ultrahigh vacuum system (CreaTec) with a base pressure of  $2.0 \times 10^{-10}$  mBar. Before STM measurement, the samples were cleaned in-situ by heating it up to 250 °C for ~3 hours.

### **Estimate the BCD from experiment**

The strength of  $D$  at each angle and gate are calculated from  $D = \frac{2\hbar^2(\sigma_{xx})^3 V_{\perp}^{2\omega} W}{e^3 \tau l^2}$ . The conductivity and relaxation time are calculated from  $\sigma_{xx} = G \frac{L}{W}$  and  $\tau = \frac{\sigma_{xx} m^*}{n e^2}$ , where  $G$  is the conductance,  $L$  is the channel length and  $m^*$  is the effective mass (see Supplementary IX for the effective mass renormalization).

### Theoretical calculation of the Berry curvature dipole

The Berry curvature dipole can be evaluated by:

$$D = -\int dk_x dk_y \sum_{\alpha, \xi} v_{\alpha k, \xi}^{x(y)} \Omega_{\alpha k, \xi} \delta_F(E_{\alpha} - E_F)$$

where  $\alpha, \xi$  are band and valley index.  $\Omega_{\alpha k, \xi} = i\langle \partial_{\mathbf{k}} u_{\alpha k, \xi} | \times | \partial_{\mathbf{k}} u_{\alpha k, \xi} \rangle$  is the BC, and  $|u_{\alpha k, \xi}\rangle$  is the Bloch wavefunction obtained from the continuum model (see supplementary VIII).  $v_{\alpha k, \xi}^{x(y)}$  is the band velocity and  $\delta_F(E_{\alpha} - E_F)$  is a delta-function centered at  $E_F$ . Detailed calculations of the BCD for strained tWSe<sub>2</sub> can be found in reference <sup>46</sup>.

## References

1. Xiao D, Chang M-C, Niu Q. Berry phase effects on electronic properties. *Rev. Mod. Phys.* **82**, 1959-2007 (2010).
2. Nagaosa N, Sinova J, Onoda S, MacDonald AH, Ong NP. Anomalous Hall effect. *Rev. Mod. Phys.* **82**, 1539-1592 (2010).
3. Xiao D, Yao W, Niu Q. Valley-contrasting physics in graphene: magnetic moment and topological transport. *Phys. Rev. Lett.* **99**, 236809 (2007).
4. Chang CZ, Zhang J, Feng X, Shen J, Zhang Z, Guo M, *et al.* Experimental observation of the quantum anomalous Hall effect in a magnetic topological insulator. *Science* **340**, 167-170 (2013).
5. Xiao D, Liu GB, Feng W, Xu X, Yao W. Coupled spin and valley physics in monolayers of MoS<sub>2</sub> and other group-VI dichalcogenides. *Phys. Rev. Lett.* **108**, 196802 (2012).
6. Wu Z, Zhou BT, Cai X, Cheung P, Liu GB, Huang M, *et al.* Intrinsic valley Hall transport in atomically thin MoS<sub>2</sub>. *Nat. Commun.* **10**, 611 (2019).
7. Sodemann I, Fu L. Quantum Nonlinear Hall Effect Induced by Berry Curvature Dipole in Time-Reversal Invariant Materials. *Phys. Rev. Lett.* **115**, 216806 (2015).
8. Zhang Y, Sun Y, Yan B. Berry curvature dipole in Weyl semimetal materials: An ab initio study. *Phys. Rev. B*. **97**, (2018).
9. Xu S-Y, Ma Q, Shen H, Fatemi V, Wu S, Chang T-R, *et al.* Electrically switchable Berry curvature dipole in the monolayer topological insulator WTe<sub>2</sub>. *Nat. Phys.* **14**, 900-906 (2018).
10. Isobe H, Xu S-Y, Fu L. High-frequency rectification via chiral Bloch electrons. *Sci. Adv.* **6**, eaay2497 (2020).
11. Selvan KV, Ali MSM. Micro-scale energy harvesting devices: Review of methodological performances in the last decade. *Renewable Sustainable Energy Rev.* **54**, 1035-1047 (2016).
12. Du ZZ, Wang CM, Lu HZ, Xie XC. Band Signatures for Strong Nonlinear Hall Effect in Bilayer WTe<sub>2</sub>. *Phys. Rev. Lett.* **121**, 266601 (2018).
13. Nandy S, Sodemann I. Symmetry and quantum kinetics of the nonlinear Hall effect. *Phys. Rev. B*. **100**, (2019).
14. Zhou BT, Zhang C-P, Law KT. Highly Tunable Nonlinear Hall Effects Induced by Spin-Orbit Couplings in Strained Polar Transition-Metal Dichalcogenides. *Phys. Rev. Applied* **13**, (2020).
15. You J-S, Fang S, Xu S-Y, Kaxiras E, Low T. Berry curvature dipole current in the transition metal dichalcogenides family. *Phys. Rev. B*. **98**, (2018).
16. Battilomo R, Scopigno N, Ortix C. Berry Curvature Dipole in Strained Graphene: A Fermi Surface Warping Effect. *Phys. Rev. Lett.* **123**, 196403 (2019).
17. Facio JI, Efremov D, Koepnick K, You J-S, Sodemann I, van den Brink J. Strongly Enhanced Berry Dipole at Topological Phase Transitions in BiTeI. *Phys. Rev. Lett.* **121**, 246403 (2018).
18. Matsyshyn O, Sodemann I. Nonlinear Hall Acceleration and the Quantum Rectification Sum Rule. *Phys. Rev. Lett.* **123**, 246602 (2019).
19. Ma Q, Xu SY, Shen H, MacNeill D, Fatemi V, Chang TR, *et al.* Observation of the nonlinear Hall effect under time-reversal-symmetric conditions. *Nature* **565**, 337-342 (2019).
20. Kang K, Li T, Sohn E, Shan J, Mak KF. Nonlinear anomalous Hall effect in few-layer WTe<sub>2</sub>. *Nat. Mater.* **18**, 324-328 (2019).
21. Son J, Kim KH, Ahn YH, Lee HW, Lee J. Strain Engineering of the Berry Curvature Dipole and Valley Magnetization in Monolayer MoS<sub>2</sub>. *Phys. Rev. Lett.* **123**, 036806 (2019).
22. Ho S-C, Chang C-H, Hsieh Y-C, Lo S-T, Huang B, Vu T-H-Y, *et al.* Zero-magnetic-field Hall effects in artificially corrugated bilayer graphene. Preprint at <https://arxiv.org/abs/1910.07509> (2019).
23. Liu J, Ma Z, Gao J, Dai X. Quantum Valley Hall Effect, Orbital Magnetism, and Anomalous Hall Effect in Twisted Multilayer Graphene Systems. *Phys. Rev. X*. **9**, (2019).

24. Wu F, Lovorn T, Tutuc E, Martin I, MacDonald AH. Topological Insulators in Twisted Transition Metal Dichalcogenide Homobilayers. *Phys. Rev. Lett.* **122**, 086402 (2019).
25. Yao W, Chen M, Yu H. Giant magnetic field from moiré induced Berry phase in homobilayer semiconductors. *Natl. Sci. Rev.* **7**, 12-20 (2020).
26. Liu J, Dai X. Anomalous Hall effect, magneto-optical properties, and nonlinear optical properties of twisted graphene systems. *npj Comput. Mater.* **6**, 57 (2020).
27. Chen X, Fan X, Li L, Zhang N, Niu Z, Guo T, *et al.* Moiré engineering of electronic phenomena in correlated oxides. *Nat. Phys.* **16**, 631-635 (2020).
28. Cao Y, Fatemi V, Fang S, Watanabe K, Taniguchi T, Kaxiras E, *et al.* Unconventional superconductivity in magic-angle graphene superlattices. *Nature* **556**, 43-50 (2018).
29. An L, Cai X, Pei D, Huang M, Wu Z, Zhou Z, *et al.* Interaction effects and superconductivity signatures in twisted double-bilayer WSe<sub>2</sub>. *Nanoscale Horiz.* **5**, 1309-1316 (2020).
30. Chen G, Sharpe AL, Gallagher P, Rosen IT, Fox EJ, Jiang L, *et al.* Signatures of tunable superconductivity in a trilayer graphene moiré superlattice. *Nature* **572**, 215-219 (2019).
31. Wang L, Shih E-M, Ghiotto A, Xian L, Rhodes DA, Tan C, *et al.* Correlated electronic phases in twisted bilayer transition metal dichalcogenides. *Nat. Mater.* **19**, 861-866 (2020).
32. Yankowitz M, Chen S, Polshyn H, Zhang Y, Watanabe K, Taniguchi T, *et al.* Tuning superconductivity in twisted bilayer graphene. *Science* **363**, 1059-1064 (2019).
33. Cao Y, Fatemi V, Demir A, Fang S, Tomarken SL, Luo JY, *et al.* Correlated insulator behaviour at half-filling in magic-angle graphene superlattices. *Nature* **556**, 80-84 (2018).
34. Chen G, Jiang L, Wu S, Lyu B, Li H, Chittari BL, *et al.* Evidence of a gate-tunable Mott insulator in a trilayer graphene moiré superlattice. *Nat. Phys.* **15**, 237-241 (2019).
35. Cao Y, Rodan-Legrain D, Rubies-Bigorda O, Park JM, Watanabe K, Taniguchi T, *et al.* Tunable correlated states and spin-polarized phases in twisted bilayer–bilayer graphene. *Nature* **583**, 215-220 (2020).
36. Chen G, Sharpe AL, Fox EJ, Zhang Y-H, Wang S, Jiang L, *et al.* Tunable correlated Chern insulator and ferromagnetism in a moiré superlattice. *Nature* **579**, 56-61 (2020).
37. Liu X, Hao Z, Khalaf E, Lee JY, Ronen Y, Yoo H, *et al.* Tunable spin-polarized correlated states in twisted double bilayer graphene. *Nature* **583**, 221-225 (2020).
38. Zhang ZM, Wang YM, Watanabe K, Taniguchi T, Ueno K, Tutuc E, *et al.* Flat bands in twisted bilayer transition metal dichalcogenides. *Nat. Phys.* (2020).
39. Auton G, Zhang J, Kumar RK, Wang H, Zhang X, Wang Q, *et al.* Graphene ballistic nano-rectifier with very high responsivity. *Nat. Commun.* **7**, 11670 (2016).
40. Kim K, Yankowitz M, Fallahazad B, Kang S, Movva HCP, Huang S, *et al.* van der Waals Heterostructures with High Accuracy Rotational Alignment. *Nano Lett.* **16**, 1989-1995 (2016).
41. Kerelsky A, McGilly LJ, Kennes DM, Xian L, Yankowitz M, Chen S, *et al.* Maximized electron interactions at the magic angle in twisted bilayer graphene. *Nature* **572**, 95-100 (2019).
42. Uri A, Grover S, Cao Y, Crosse JA, Bagani K, Rodan-Legrain D, *et al.* Mapping the twist-angle disorder and Landau levels in magic-angle graphene. *Nature* **581**, 47-52 (2020).
43. Zhang Y-H, Po HC, Senthil T. Landau level degeneracy in twisted bilayer graphene: Role of symmetry breaking. *Phys. Rev. B.* **100**, 125104 (2019).
44. Jiang Y, Lai X, Watanabe K, Taniguchi T, Haule K, Mao J, *et al.* Charge order and broken rotational symmetry in magic-angle twisted bilayer graphene. *Nature* **573**, 91-95 (2019).
45. Du ZZ, Wang CM, Li S, Lu HZ, Xie XC. Disorder-induced nonlinear Hall effect with time-reversal symmetry. *Nat. Commun.* **10**, 3047 (2019).
46. Hu J-X, Zhang C-P, Xie Y-M, Law KT. Nonlinear Hall Effects in Strained Twisted Bilayer WSe<sub>2</sub>. Preprint at <https://arxiv.org/abs/2004.14140> (2020).
47. Das Sarma S, Wu F. Electron–phonon and electron–electron interaction effects in twisted bilayer graphene. *Ann. Phys.* **417**, 168193 (2020).
48. Po HC, Zou L, Vishwanath A, Senthil T. Origin of Mott Insulating Behavior and Superconductivity in Twisted Bilayer Graphene. *Phys. Rev. X* **8**, 031089 (2018).



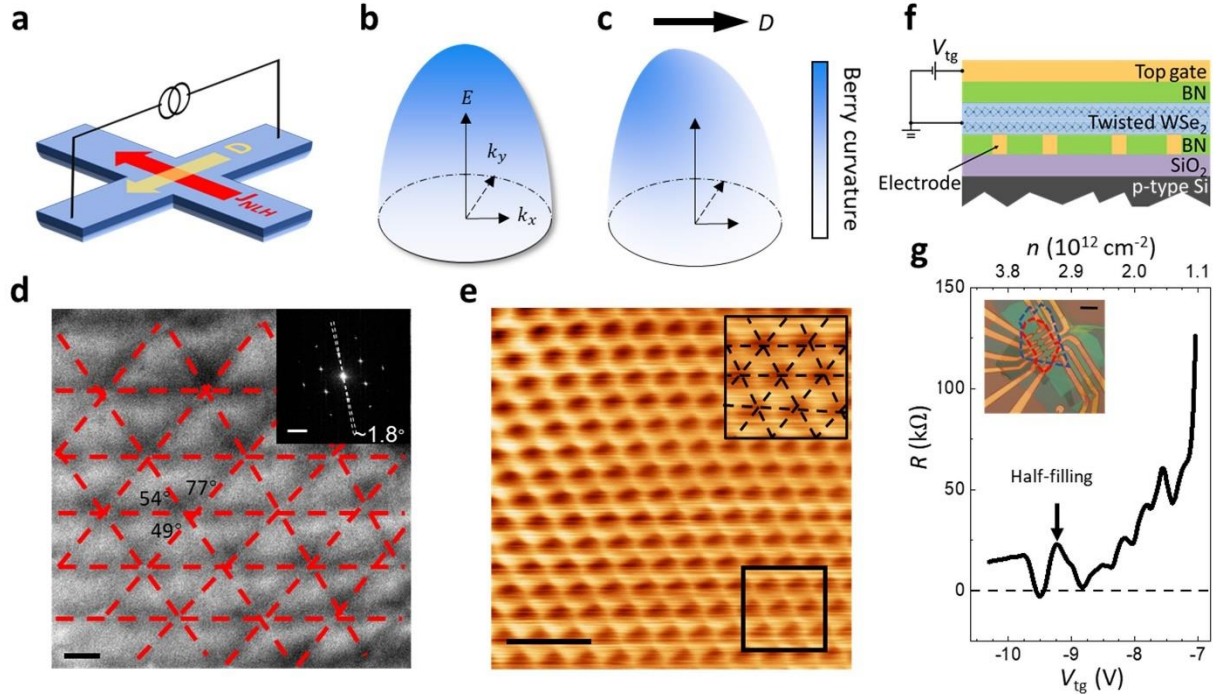
49. Brinkman WF, Rice TM. Application of Gutzwiller's Variational Method to the Metal-Insulator Transition. *Phys. Rev. B.* **2**, 4302-4304 (1970).
50. Senatore G, De Palo S. Correlation effects in low dimensional electron systems: the electron-hole bilayer. *Contrib. Plasma Phys.* **43**, 363-368 (2003).

## Acknowledgements

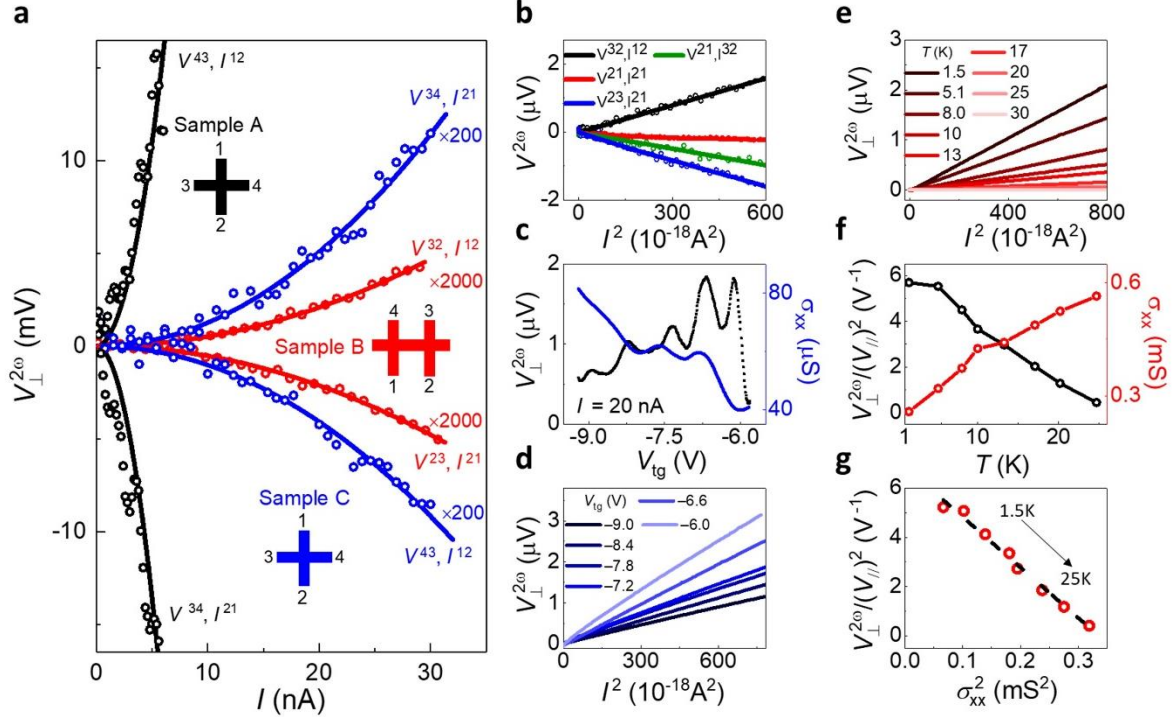
We first thank Inti Sodemann and Oles Matsyshyn for insightful advices. We also thank Prof. Z. Y. Yang, Dr. Qinsheng Wang and Dr. Benjamin T. Zhou for fruitful discussions on experiments and theoretical analysis. Great supports from the National Key R&D Program of China (2020YFA 0309600) and the Research Grants Council (RGC) of Hong Kong (Project No. 16300717 and C7036-17W) are acknowledged. E.L. and N.L. thank the RGC funding of Hong Kong (CRF No. C6012-17E). Device fabrication was performed at the MCPF and WMINST of HKUST with technical support from Ms. Wing Ki Wong and Dr. Yuan Cai.

## Author contributions

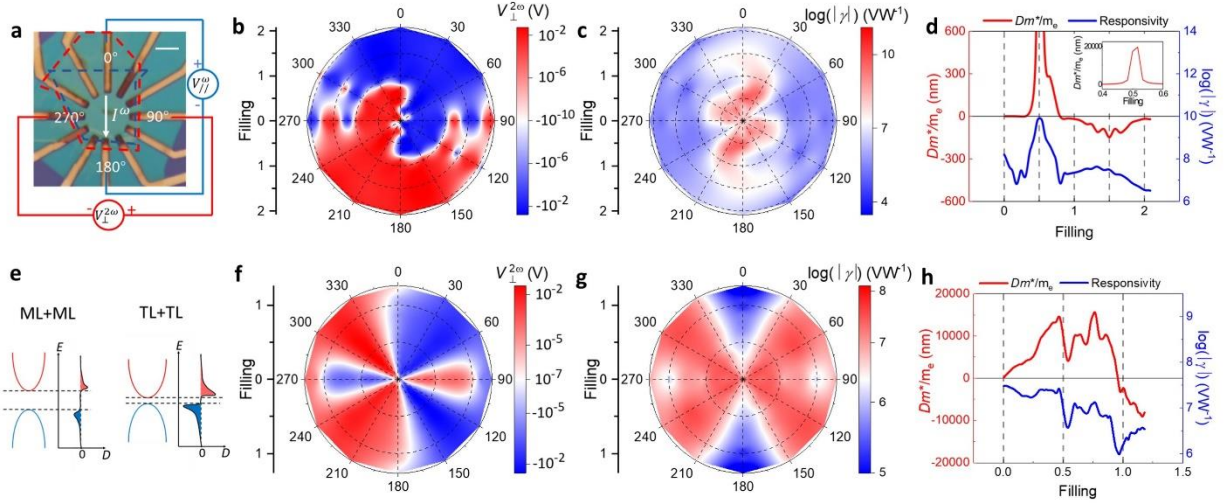
N.W. and K.-T.L. supervised the work. Z.-F.W. and M.-Z.H. conceived the project and designed the experiments. M.-Z.H. and Z.-F.W. fabricated the devices, performed the measurements and analyzed the data. L.-H.A., X.-M.F. and Z.-Q.Y. provided technical help in the device fabrication process. X.-B.C. performed STEM characterizations. E.L. performed STM characterizations under the supervision of N.L. J.-X.H. computed the Band structures, Berry curvatures and Berry curvature dipoles under the supervision of K.-T.L. Then, Z.-F.W., M.-Z.H. and J.-X.H. analyzed the computational results and wrote theoretical explanations. Z.-F.W., M.-Z.H., N.W. and K.-T.L. wrote the manuscript.



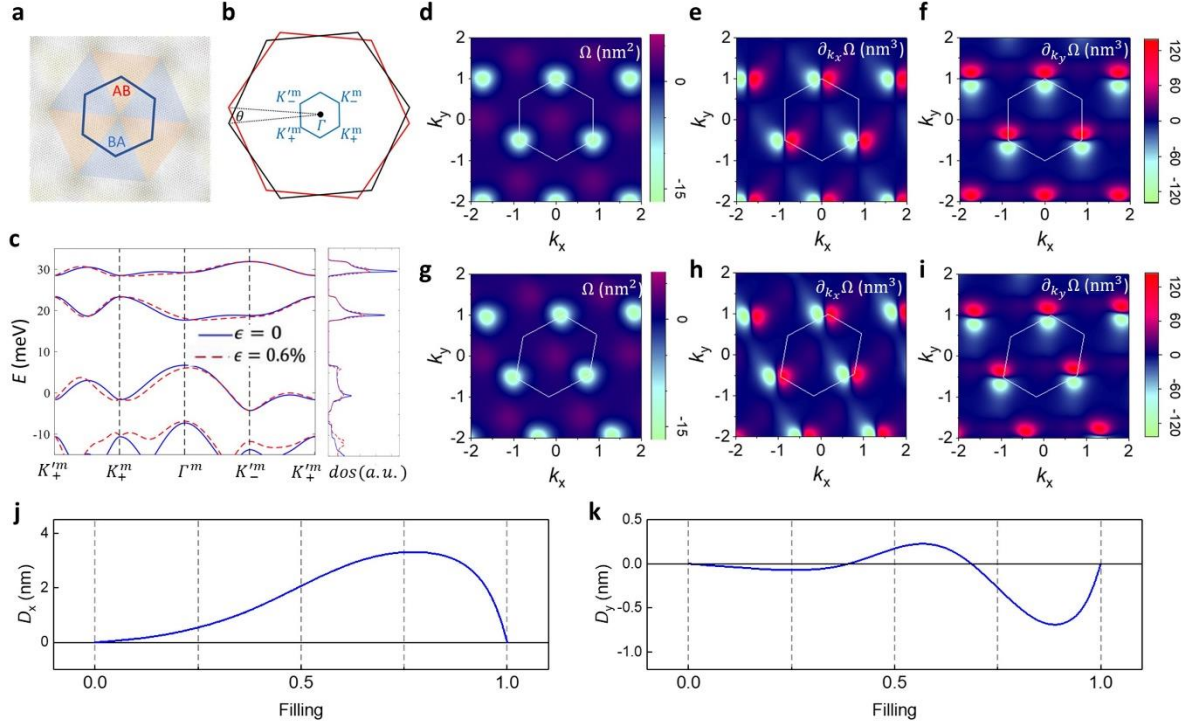
**Fig.1 | Electron microscope and transport characterizations of twisted WSe<sub>2</sub>.** **a**, Illustration of the nonlinear Hall effect. An external AC electric field parallel to the Berry curvature dipole  $D$  can generate both a DC and second harmonic nonlinear Hall current  $J_{NLH}$ . **b**, Schematic band structure and Berry curvature of the K valley. The intrinsically broken inversion symmetry induces non-zero Berry curvature near the moiré valence band edge. **c**, Strain tilts the band dispersion, allowing the states at the Fermi level to have non-uniform Berry curvature amplitude, and the non-zero Berry curvature dipole. **d**, High-resolution STEM image of the moiré superlattice formed from twisted WSe<sub>2</sub> (scale bar 5 nm). AA stacking points (W atom on W atom or Se atom on Se atom) are connected through red lines. The distorted triangular moiré demonstrates the broken spatial symmetry. Inset: Diffraction pattern taken from the sample indicates a 1.8° twist angle (scale bar 2.3 nm<sup>-1</sup>). **e**, STM image from twisted WSe<sub>2</sub> (scale bar 20 nm). Inset: Enlarged image of the region marked by the dark square (area length 19.2 nm). The moiré unit cells are deviated from a hexagonal pattern. For example, the enlarged pattern in the dark square area is a scalene hexagon. **f**, Schematic of device structure. **g**, Resistance plotted as functions of  $V_{tg}$  and  $n$  for our twisted double bilayer WSe<sub>2</sub> sample with a twist angle of  $3.1 \pm 0.2^\circ$  (sample B). Inset: Optical image of a tWSe<sub>2</sub> device before top gate deposition (scale bar 8 μm). Red (blue) dashed areas correspond to top (bottom) WSe<sub>2</sub>.



**Fig.2 | Nonlinear transport of twisted WSe<sub>2</sub>.** Data in (a)-(d) are measured at  $T=1.5$  K. **a**, Second harmonic Hall voltages measured in different samples (black: sample A (1L+1L), blue: sample B (2L+2L), red: sample C (3L+3L)).  $V^{43}$  and  $I^{12}$  indicate that the second harmonic voltage is measured through probes 4 and 3 when current ( $I$ ) is injected through probes 1 and 2. The dots are experimental data and the solid lines are parabolic fits of the data. Insets: Schematics of the electrode geometry. **b**, Second harmonic voltages measured in sample B using different combinations of electrodes as a function of the square of current amplitude at  $V_{tg} = -8.2$  V. **c**, Second harmonic Hall voltages (left, black) at fixed current amplitude  $I = 20$  nA and longitude conductance (right, blue) as a function of gate voltage. The data in (c)-(g) are measured in sample B using the same configuration in (a). **d**, Second harmonic Hall voltages measured at different gates as functions of the square of current amplitude. **e**,  $V_{\perp}^{2\omega}$  measured at different temperatures as a function of  $I^2$ . **f**, Fitted  $V_{\perp}^{2\omega}/(V_{\parallel})^2$  (left, black) and longitude conductivity  $\sigma_{xx}$  (right, red) as a function of temperature. **g**,  $V_{\perp}^{2\omega}/(V_{\parallel})^2$  as a function of  $(\sigma_{xx})^2$  at different temperatures. The dashed line is a linear fitting of experiment data. Data in (e)-(g) are measured at  $V_{tg} = -8.2$  V.



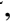
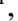

**Fig. 3 | Angular-dependent nonlinear Hall effect.** **a**, Optical image of a  $2.0 \pm 0.2^\circ$  twisted double-monolayer WSe<sub>2</sub> sample (sample A) with 12 electrodes in a circle (scale bar  $4 \mu\text{m}$ ). Blue (red) dashed areas correspond to top (bottom) WSe<sub>2</sub>. Angular dependent nonlinear Hall effect was measured by injecting a current from the electrode at angle  $\theta$  (from crystal edge) to electrode at angle  $\theta + 180^\circ$ .  $V_\perp^{2\omega}$  was set as the potential at  $\theta + 90^\circ$  minus the potential at  $\theta + 270^\circ$ . **b**, **c**, Angular and filling factor dependences of  $V_\perp^{2\omega}$  (**b**), responsivity  $\gamma$  (**c**) measured from the nonlinear Hall effect in sample A at  $T = 1.5 \text{ K}$ . The  $V_\perp^{2\omega}$  mapping shows two kinds of regions marked with red (positive value) and blue (negative value). **d**,  $Dm^*$  and  $\gamma$  versus the filling factor in sample A at  $\theta = 0^\circ$ . Inset:  $Dm^*$  versus filling factor plotted in large scale. **e**, Schematic band structure of the hole moiré band and the dipole amplitude at different Fermi levels in tWSe<sub>2</sub> with different layer numbers. The dipole has opposite signs in different moiré bands and is zero in the band gap. **f**, **g**, Angular and filling factor dependences of  $V_\perp^{2\omega}$  (**f**),  $\gamma$  (**g**) measured in twisted double-trilayer WSe<sub>2</sub> (sample C) at  $T = 1.5 \text{ K}$ . Data shown in (b), (c), (f) and (g) are average values of the data at  $\theta$  and  $\theta + 180^\circ$ . **h**,  $Dm^*$  and  $\gamma$  versus filling factor in sample C (**i**) at  $\theta = 90^\circ$ .



**Fig. 4 | Theoretical modelling of strain-induced Berry curvature dipole.** **a**, A perfect superlattice formed from twisted bilayer WSe<sub>2</sub> with D<sub>3</sub> point group symmetry. The blue line indicates the moiré Brillouin zone. W atom on Se atom or Se atom on W atom are labeled by AB domain and BA domain. **b**, First Brillouin zone of the top layer (black), bottom layer (red) WSe<sub>2</sub> and the moiré Brillouin zone (blue). **c**, Band structure and density of states without (blue) and with (red) strain along zigzag direction in twisted bilayer WSe<sub>2</sub>. The displacement electric field is set at 10 meV in the calculation in (c)-(k). **d**, The Berry curvature of the top moiré valence band without strain. **e-f**, Dipole density along  $k_x$  (e) and  $k_y$  (f) directions without any strain.  $k_x$  and  $k_y$  are in units of nm<sup>-1</sup>. **g-i**, The Berry curvature (g), dipole density along  $k_x$  (h) and  $k_y$  (i) direction after introducing a strain strength of 0.6% along zigzag direction. **j, k**, Theoretical values of  $D$  plotted as a function of filling factor based on a non-interacting model.  $D_x$  (j) and  $D_y$  (k) are the BCD along the zigzag and armchair directions respectively.

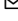
# Supplementary Information

## Giant nonlinear Hall effect in twisted WSe<sub>2</sub>

Meizhen Huang<sup>1,2</sup>, Zefei Wu<sup>1,2</sup> , Jinxin Hu<sup>1,2</sup>, Xiangbin Cai<sup>1</sup>, En Li<sup>1</sup>, Liheng An<sup>1</sup>, Xuemeng Feng<sup>1</sup>, Ziqing Ye<sup>1</sup>, Nian Lin<sup>1</sup>, Kam Tuen Law<sup>1</sup> , Ning Wang<sup>1</sup> 

<sup>1</sup>Department of Physics and Center for Quantum Materials, The Hong Kong University of Science and Technology, Hong Kong, China

<sup>2</sup>These authors contributed equally: Meizhen Huang, Zefei Wu, Jinxin Hu.

 e-mail: phwang@ust.hk; phlaw@ust.hk; wzefei@connect.ust.hk

### Content

I.	Obtaining local strain from STEM and STM images .....	2
II.	Determine twist angles from transport data .....	6
III.	Superconducting signatures in sample B .....	8
IV.	Additional transport data.....	9
V.	Analysis of the temperature dependent nonlinear Hall effect .....	13
VI.	Angular dependent nonlinear Hall effect .....	14
VII.	Dipole, responsivity and noise equivalent power .....	15
VIII.	The continuum model .....	18
IX.	Effective mass renormalization.....	20
X.	Interaction induced gapped phase at the half filling .....	22
XI.	Comparison between twisted WSe <sub>2</sub> and monolayer WSe <sub>2</sub> .....	24
XII.	Origin of the symmetry breaking. ....	25
XIII.	Calculation of the displacement electric field.....	26
XIV.	The effects of strain and displacement electric field on BCD.....	27

## I. Obtaining local strain from STEM and STM images

### a. Uniaxial heterostrain model for twisted WSe<sub>2</sub>

Though the strain in artificially constructed samples can be quite complex, uniaxial or multiaxial, uniform or with gratitute, a uniaxial heterostrain model is used to obtain the local strain<sup>1</sup>. The real space moiré wavelengths can be described as

$$|M_{N=1,2,3}| = \frac{4\pi}{\sqrt{3}|k'_N - k_{Ns}|} \quad (1)$$

where  $N = 1,2,3$  denotes the three directions in reciprocal space,  $k'_N$  is the reciprocal wavelength after rotated at twist angle  $\theta_T$  and  $k_{Ns}$  is the reciprocal wavelength for the strained lattice. They can be achieved by the matrix

$$k'_N = \begin{pmatrix} \cos \theta_T & -\sin \theta_T \\ \sin \theta_T & \cos \theta_T \end{pmatrix} k_N \quad (2)$$

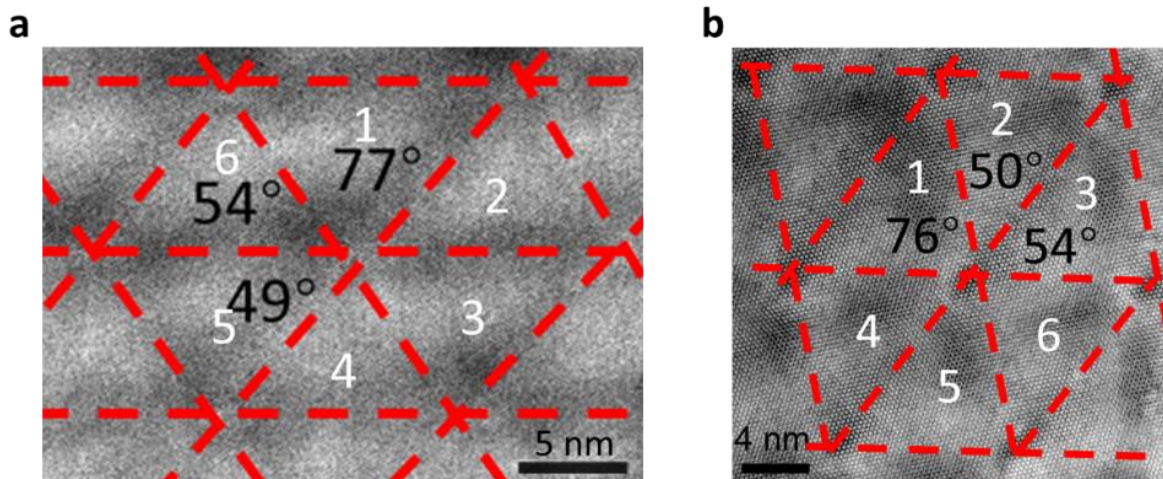
and

$$k_{Ns} = \begin{pmatrix} \cos \theta_S & \sin \theta_S \\ -\sin \theta_S & \cos \theta_S \end{pmatrix} \begin{pmatrix} \frac{1}{1+\varepsilon} & 0 \\ 0 & \frac{1}{1-\delta\varepsilon} \end{pmatrix} \begin{pmatrix} \cos \theta_S & -\sin \theta_S \\ \sin \theta_S & \cos \theta_S \end{pmatrix} k_N \quad (3)$$

where  $\delta = 0.19$  is the Poisson ratio<sup>2</sup> of WSe<sub>2</sub>,  $\varepsilon$  is the strain strength, and strain is applied at an angle  $\theta_S$  to one of the WSe<sub>2</sub> lattice.  $k_1 = \begin{pmatrix} k \\ 0 \end{pmatrix}$ ,  $k_2 = \begin{pmatrix} k \cos 60^\circ \\ k \sin 60^\circ \end{pmatrix}$ ,  $k_3 = \begin{pmatrix} k \cos 120^\circ \\ k \sin 120^\circ \end{pmatrix}$  is the reciprocal wavevectors, and  $k = \frac{4\pi}{\sqrt{3}a_0}$  is calculated using the lattice constant  $a_0 = 0.33$  nm of WSe<sub>2</sub>. The strain strength can be calculated from the distance between three nearest AA points in each triangle in the STEM and STM image.

### b. Strain in STEM image





**Supplementary Fig. 1 | Lattice distortion in STEM sample. a,** An enlarged area in Fig. 1d (scale bar 5 nm). **b,** Another enlarged area from the same sample (scale bar 4 nm).

**Supplementary Table. 1 | Strain calculated from supplementary Fig. 1a.**

No.	$ M_1 $ ( $\pm 0.3\text{nm}$ )	$ M_2 $ ( $\pm 0.3\text{nm}$ )	$ M_3 $ ( $\pm 0.3\text{nm}$ )	$\theta_T$ ( $\pm 0.1^\circ$ )	$\theta_S$ ( $^\circ$ )	$\varepsilon$ (%)
1	13.37	9.49	10.62	1.69	61.68	1.13
2	12.04	8.99	10.62	1.78	68.92	1.08
3	12.04	8.99	10.71	1.77	69.85	1.09
4	10.91	8.99	9.89	1.90	64.02	0.73
5	11.55	9.68	9.89	1.82	51.16	0.65
6	11.55	9.49	9.88	1.83	54.21	0.72
Average				1.80	61.64	0.90

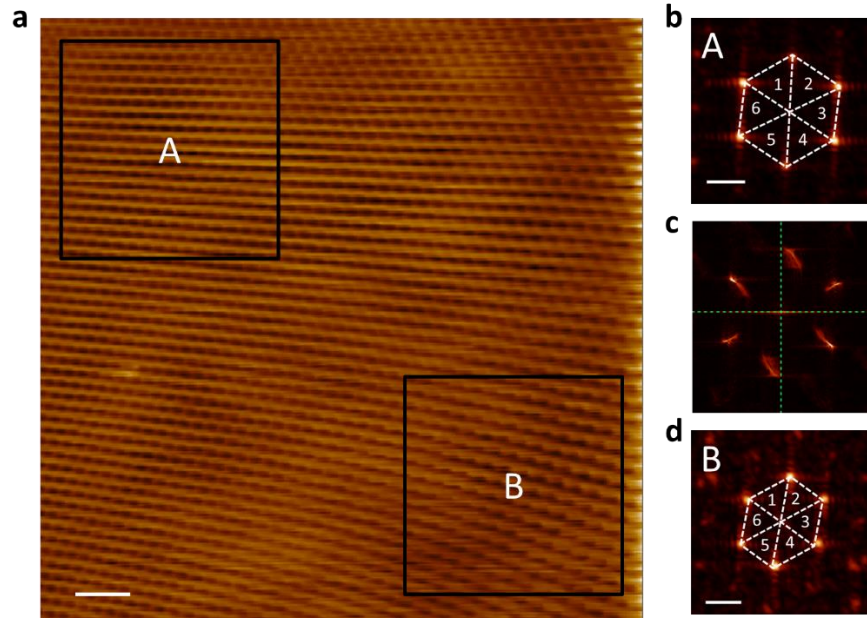
**Supplementary Table. 2 | Strain calculated from supplementary Fig. 1b.**

No.	$ M_1 $ ( $\pm 0.3\text{nm}$ )	$ M_2 $ ( $\pm 0.3\text{nm}$ )	$ M_3 $ ( $\pm 0.3\text{nm}$ )	$\theta_T$ ( $\pm 0.1^\circ$ )	$\theta_S$ ( $^\circ$ )	$\varepsilon$ (%)
1	14.47	12.10	10.22	1.54	31.59	1.03
2	14.82	12.10	10.55	1.51	35.29	1.02
3	14.82	12.08	10.87	1.50	37.31	0.91
4	12.39	10.75	10.22	1.70	39.05	0.64
5	12.39	10.48	10.61	1.69	49.51	0.59
6	12.40	10.48	10.87	1.68	54.11	0.56
Average				1.60	41.14	0.80



For the STEM image, the strain in supplementary Fig. 1a and 1b are calculated, as shown in supplementary table. 1 and 2, respectively. The average strain strength is 0.90% in supplementary Fig. 1a and 0.80% in supplementary Fig. 1b. The strain inhomogeneity is confirmed by the different strain strength obtained at each triangle, the different average strain at different sample areas and the inhomogeneous contrast inside each triangle.

c. Strain in STM image



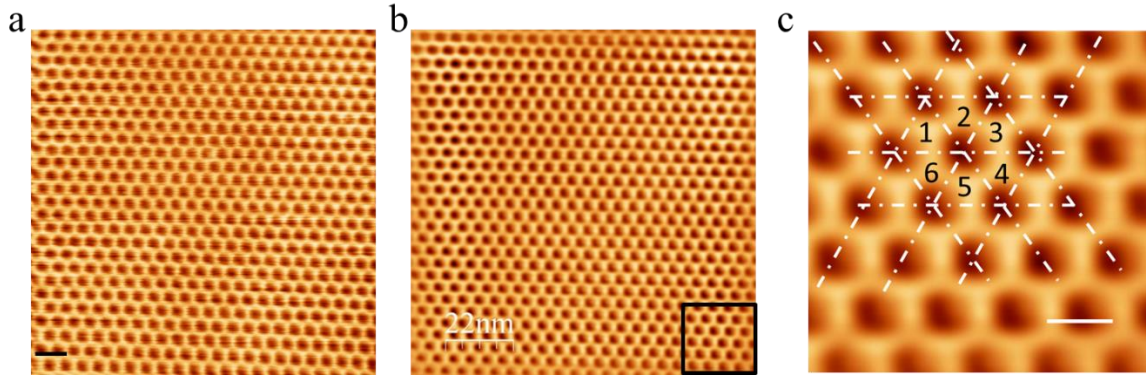
**Supplementary Fig. 2 | Lattice distortion in STM sample 1.** **a**, Original unfiltered large area STM image from tWSe<sub>2</sub> (scale bar 25 nm). **b**, FFT pattern from the dark square area A in **(a)**, the scale bar is 0.54 nm<sup>-1</sup>. **c**, FFT pattern from a 300 nm × 300 nm large area **(a)**. **d**, FFT pattern from the dark square area B in **(a)**, the scale bar is 0.54 nm<sup>-1</sup>.

**Supplementary Table. 3 | Strain calculated from area A in Supplementary Fig. 2.**

No.	$ M_1 $ ( $\pm 0.3\text{nm}$ )	$ M_2 $ ( $\pm 0.3\text{nm}$ )	$ M_3 $ ( $\pm 0.3\text{nm}$ )	$\theta_T$ ( $\pm 0.1^\circ$ )	$\theta_S$ ( $^\circ$ )	$\varepsilon$ (%)
1	10.51	10.36	9.88	1.84	21.53	0.24
2	10.03	9.73	9.88	1.91	59.91	0.11
3	10.03	10.66	10.34	1.83	30.03	0.22
4	10.47	10.66	9.78	1.84	10.71	0.33
5	9.77	9.89	9.78	1.93	19.11	0.05
6	9.77	10.36	10.07	1.88	30.69	0.21
Average				1.87	28.66	0.20

**Supplementary Table. 4 | Strain calculated from area B in Supplementary Fig. 2.**

No.	$ M_1 $ ( $\pm 0.3\text{nm}$ )	$ M_2 $ ( $\pm 0.3\text{nm}$ )	$ M_3 $ ( $\pm 0.3\text{nm}$ )	$\theta_T$ ( $\pm 0.1^\circ$ )	$\theta_S$ ( $^\circ$ )	$\varepsilon$ (%)
1	9.52	10.72	9.45	1.91	11.77	0.51
2	9.74	11.00	9.45	1.88	6.92	0.57
3	9.74	11.51	9.94	1.82	16.43	0.62
4	9.76	11.51	9.53	1.84	8.64	0.70
5	9.50	11.21	9.53	1.87	13.34	0.66
6	9.50	10.72	9.40	1.91	11.07	0.53
Average				1.87	11.36	0.60

**Supplementary Fig. 3 | Lattice distortion in STM sample 2. a,** Original unfiltered data for STM sample 2 (scale bar 10 nm). **b,** Filtered STM image from STM sample 2 (scale bar 22 nm). **c,** Enlarged image from the dark square in (a), the scale bar is 5 nm.**Supplementary Table. 5 | Strain calculated from STM sample 2 (shown in Supplementary Fig. 3c).**

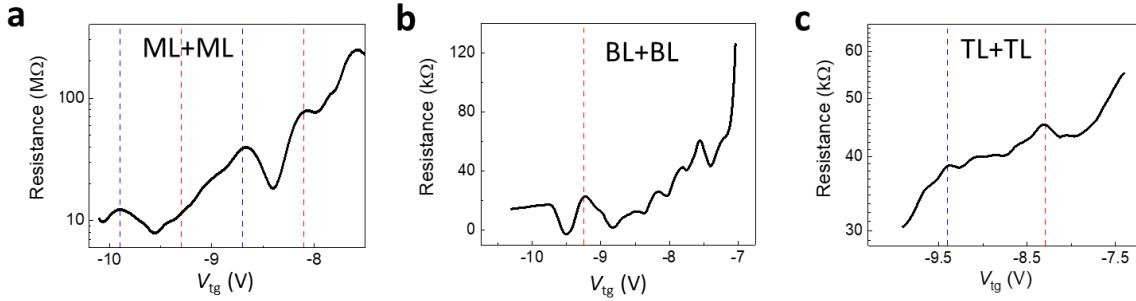
No.	$ M_1 $ ( $\pm 0.3\text{nm}$ )	$ M_2 $ ( $\pm 0.3\text{nm}$ )	$ M_3 $ ( $\pm 0.3\text{nm}$ )	$\theta_T$ ( $\pm 0.1^\circ$ )	$\theta_S$ ( $^\circ$ )	$\varepsilon$ (%)
1	4.78	5.05	5.25	3.77	56.25	0.61
2	4.85	5.05	5.30	3.73	61.01	0.56
3	4.85	5.22	5.44	3.66	54.16	0.73
4	4.70	4.97	5.44	3.74	24.94	0.92
5	4.62	4.97	5.28	3.82	56.72	0.88
6	4.62	4.92	5.25	3.84	58.54	0.83
Average				3.76	51.94	0.76

**Supplementary Table. 6 | Strain calculated from STM sample 3 (shown in inset of Fig. 1e).**

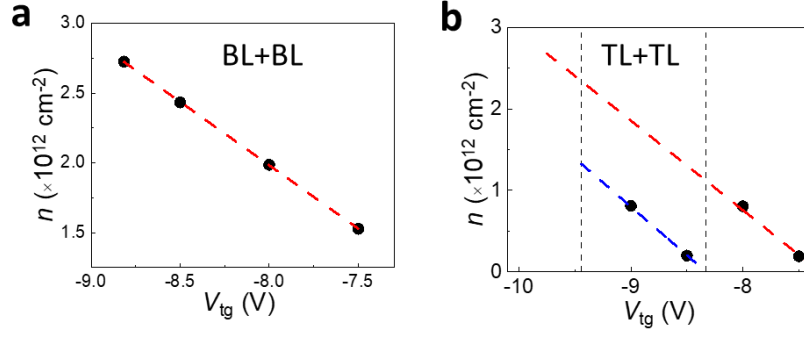
No.	$ M_1  (\pm 0.3\text{nm})$	$ M_2  (\pm 0.3\text{nm})$	$ M_3  (\pm 0.3\text{nm})$	$\theta_T (\pm 0.1^\circ)$	$\theta_S (^\circ)$	$\varepsilon (\%)$
1	8.97	8.42	9.46	2.11	4.23	0.42
2	9.82	8.42	9.87	2.01	16.98	0.65
3	9.82	7.94	9.75	2.05	19.16	0.91
4	10.12	8.63	9.75	1.99	23.09	0.58
5	9.43	8.63	9.54	2.05	14.03	0.39
6	9.43	8.51	9.46	2.07	16.25	0.44
Average				2.05	15.62	0.57

From the STM study, the moiré superlattice shown in supplementary Fig. 2a are highly distorted and show inhomogeneous strain strength. The FFT patterns from the local area illustrate similar behaviour. The strain strength obtained from area A is 0.20% while the strain strength in area B is 0.60%. The twist angle is determined to be  $1.87 \pm 0.1^\circ$  in this sample. For the STM sample shown in supplementary Fig. 3 (sample 2) and the STM sample shown in Fig. 1e (sample 3), we observe similar distortion behaviour. The twist angle and the strain strength are calculated to be  $3.76 \pm 0.1^\circ$  and 0.76% in sample 2. For sample 3, The twist angle and the strain strength are calculated to be  $2.05 \pm 0.1^\circ$  and 0.57%.

## II. Determine twist angles from transport data



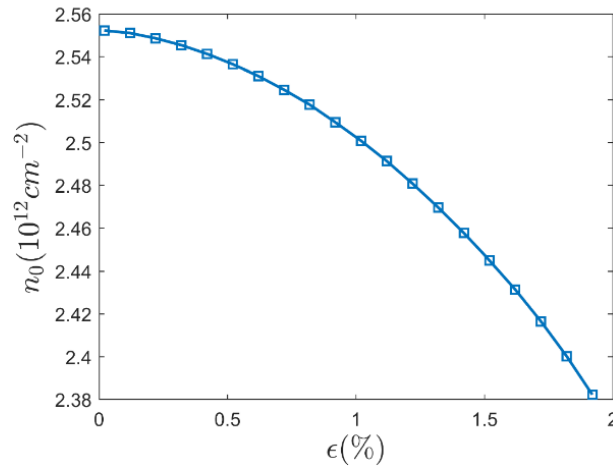
**Supplementary Fig. 4 | Transport data in different samples. a,** Resistance in sample A. **b,** Resistance in sample B. **c,** Resistance in sample C. Red dashed lines represent the half filling and the blue dashed lines represent the full filling.



**Supplementary Fig. 5 | Hall resistance determined carrier density in different samples. a,** Carrier density versus gate voltage in sample B. **b,** Carrier density versus gate voltage in sample C. Dots are measured values and lines are linear fittings of the data.

The twist angles can be determined by the carrier density at the full filling of the moiré unit cell based on  $n_0 = 2/\left(\frac{\sqrt{3}}{2}\lambda^2\right)$  where  $\lambda = a/(2 \sin \frac{\theta}{2})$  is the moiré superlattice constant calculated using the lattice constant of WSe<sub>2</sub>  $a = 0.33 \text{ nm}$ .

Since the strain can change the lattice constant slightly and further change the carrier density. In Supplementary Fig. 6, we depict the carrier density of the full filling  $n_0$  with increasing the strain strength  $\epsilon$  for twisted WSe<sub>2</sub> with a twist angle of  $2^\circ$  by using the heterostrain model<sup>3</sup>. From the calculation, the carrier density of full filling is found to change only 2% when the strain reaches 1%. Therefore, our experimental results are within a reasonable error range.



**Supplementary Fig. 6 | Carrier density of full filling as a function of strain strength.**

The carrier density at the full filling can be determined by a combination of the Hall measurement and carrier density induced by  $V_{tg}$  based on a capacitor model:

$$ne = C(V_{\text{tg}} - V_0) = \frac{\epsilon_r \epsilon_0}{d}(V_{\text{tg}} - V_0) \quad (4)$$

where  $C$  is the capacitance of the top BN,  $\epsilon_r$  and  $\epsilon_0$  denote relative and vacuum dielectric constant respectively,  $d$  is the thickness of the top BN.  $V_0$  is the threshold voltage at which the Fermi level touches the flat band edge.

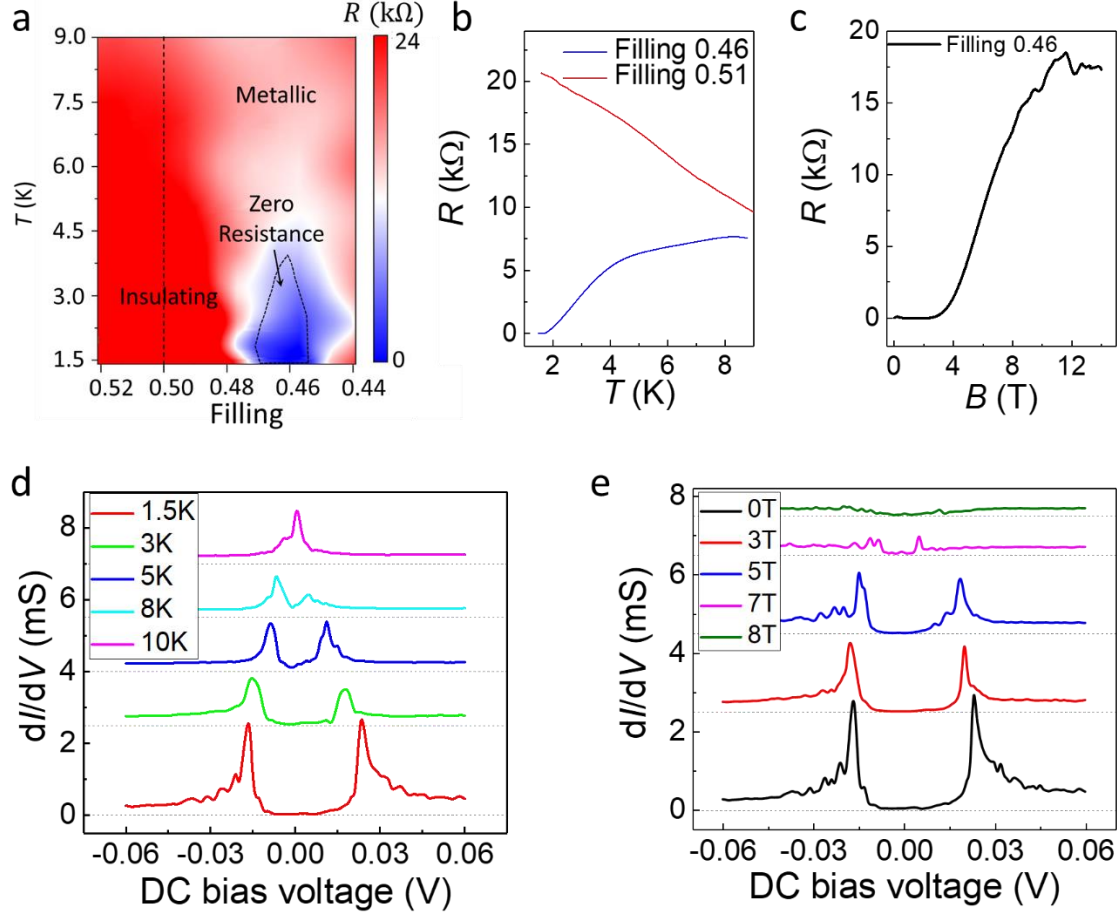
a) For our sample A (twisted double-monolayer WSe<sub>2</sub>), the resistance as a function of gate voltages is shown in supplementary Fig. 4a. Two peaks have been observed at  $V_{\text{tg}} = -8.7$  V and  $V_{\text{tg}} = -9.9$  V. Using the thickness of the top BN (10 nm), the gate capacitance is calculated to be  $C_1 = 0.00345$  F m<sup>-2</sup>. The twist angle of  $2.0 \pm 0.2^\circ$  can be determined from the carrier density at  $V_{\text{tg}} = -8.7$  V ( $n = 2.61 \times 10^{12}$  cm<sup>-2</sup>) and  $V_{\text{tg}} = -9.9$  V ( $n = 5.23 \times 10^{12}$  cm<sup>-2</sup>).

b) For our sample B (twisted double-bilayer WSe<sub>2</sub>), the resistance and the measured carrier density are shown in Supplementary Fig. 4b and 5a, respectively. The gate capacitance obtained from the slope of the red line in Supplementary Fig. 5a  $C_2 = 0.00147$  F m<sup>-2</sup> matches well with the capacitance  $C_3 = 0.00151$  F m<sup>-2</sup> calculated from the thickness of the top BN (19.4 nm). The twist angle of  $3.1 \pm 0.2^\circ$  can be determined from the carrier density at  $V_{\text{tg}} = -9.2$  V ( $V_0 = -5.82$  V,  $n = 3.08 \times 10^{12}$  cm<sup>-2</sup>).

c) For our sample C (twisted double-trilayer WSe<sub>2</sub>), the resistance as a function of gate voltages is shown in supplementary Fig. 4c. Two peaks have been observed at  $V_{\text{tg}} = -8.3$  V and  $V_{\text{tg}} = -9.4$  V. The dots shown in supplementary Fig. 5b is the carrier density extracted from Hall measurement.  $V_{\text{tg}} = -8.3$  V should be the half filling of the superlattice since the carrier density resets to nearly zero after passing that gate voltage<sup>4</sup>, instead of monotonically increasing with gate voltage. The red line is the linear fitting of  $n$  before the half filling and can be viewed as the total  $n$  induced by the  $V_{\text{tg}}$ . The gate capacitance obtained from the slope of the red line  $C_4 = 0.00192$  F m<sup>-2</sup> is almost the same with  $C_5 = 0.00193$  F m<sup>-2</sup> calculated from the thickness of BN (18 nm). This consistence can exclude the possibility that  $V_{\text{tg}} = -8.3$  V is the full filling of the superlattice in our sample. The blue line is a linear fitting of  $n$  between the resistance peaks, it has almost the same slope as the red line. Since the total  $n$  at  $V_{\text{tg}} = -9.4$  V is the twice the density of that at  $V_{\text{tg}} = -8.3$  V, it can be viewed as the full filling of the superlattice. The twist angle of sample B is then determined to be  $2.0 \pm 0.2^\circ$ .

### III. Superconducting signatures in sample B

The superconducting signatures are observed near the half filling. Supplementary Fig. 7a and Fig. 7b shows the four-probe resistance as a function of filling factor and temperature. The resistance decreasing (increasing) with increasing temperature highlights the half filling (correlated metallic) of the superlattice. Magnetic field dependent resistance at the correlated metallic state is shown in Supplementary Fig. 7c. The resistance increases and saturates when increases the magnetic field. Differential conductance  $dI/dV$  versus DC bias voltage at different temperatures and different values of magnetic field is shown in Supplementary Fig. 7d and 7e. The two differential conductance peaks gradually suppressed with increasing temperature and magnetic field highlights the superconducting signatures.

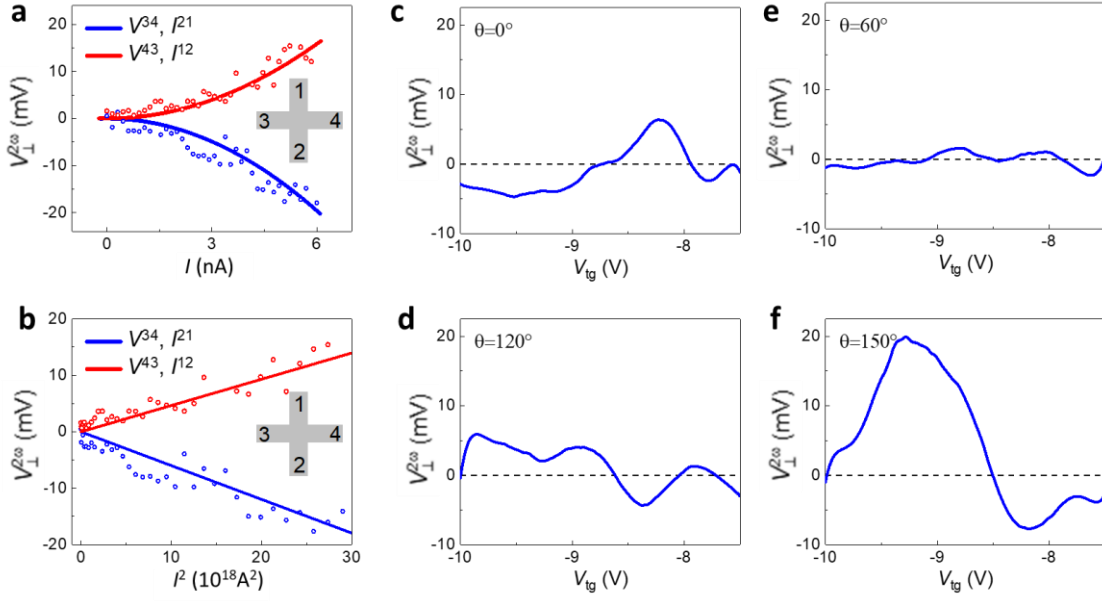


**Supplementary Fig. 7 | Half-filling of the superlattice and correlated metallic states in sample B.** **a**, Four-probe resistance as a function of filling factor and temperature. **b**, Four-probe resistance as a function of temperature at filling 0.46 and 0.51. **c**, Field response of the resistance. **d**,  $dI/dV$  versus DC bias voltage at different temperatures. **e**,  $dI/dV$  versus DC bias voltage at different magnetic field.

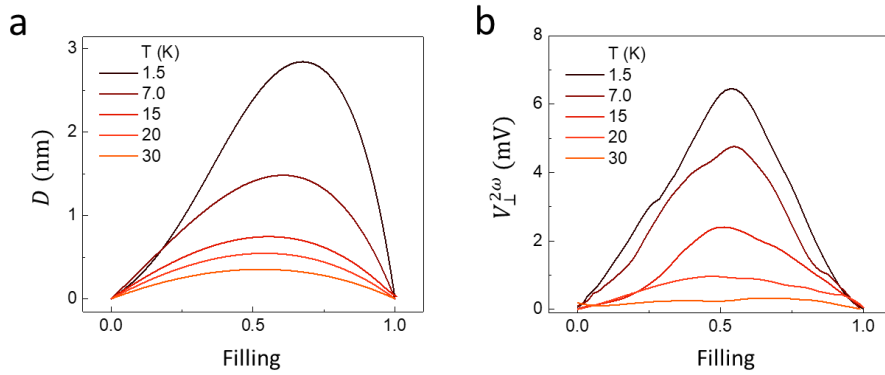
#### IV. Additional transport data

We have measured 10 twisted WSe<sub>2</sub> devices with different twist angles and layer numbers. Qualitatively, all these devices exhibit nonlinear Hall effect. Quantitatively, for the same sample, the measured second harmonic Hall voltage does not change in repeated measurements. For different samples, they show different dipole and responsivity values due to different twist angles and strain strength. For the samples constructed with the same layer numbers (for example, twisted bilayer) and different twist angles, we observed smaller nonlinear Hall signals in the samples with larger twist angles.

##### a. Additional transport data in sample A



**Supplementary Fig. 8 | Other nonlinear transport data in sample A at T=1.5K.** **a,b,** Second harmonic Hall voltage measured from different combinations of electrodes as functions of current amplitude and the square of current amplitude at gate voltage  $V_{tg} = -9.25$  V. Dots are measured value and lines are fitted curves. Inset: electrode configuration of the device. The Hall voltage which scales quadratically with inject current demonstrate the nonlinear Hall effect. **c-f,** Second harmonic Hall voltage measured at different current injection directions as a function of gate voltage.



**Supplementary Fig. 9 | Temperature-dependent nonlinear Hall effect in sample A.** **a,** Theoretical calculated Berry curvature dipole as a function of fillings at different temperature. **b,** Measured second harmonic Hall voltage as a function of fillings at different temperature.

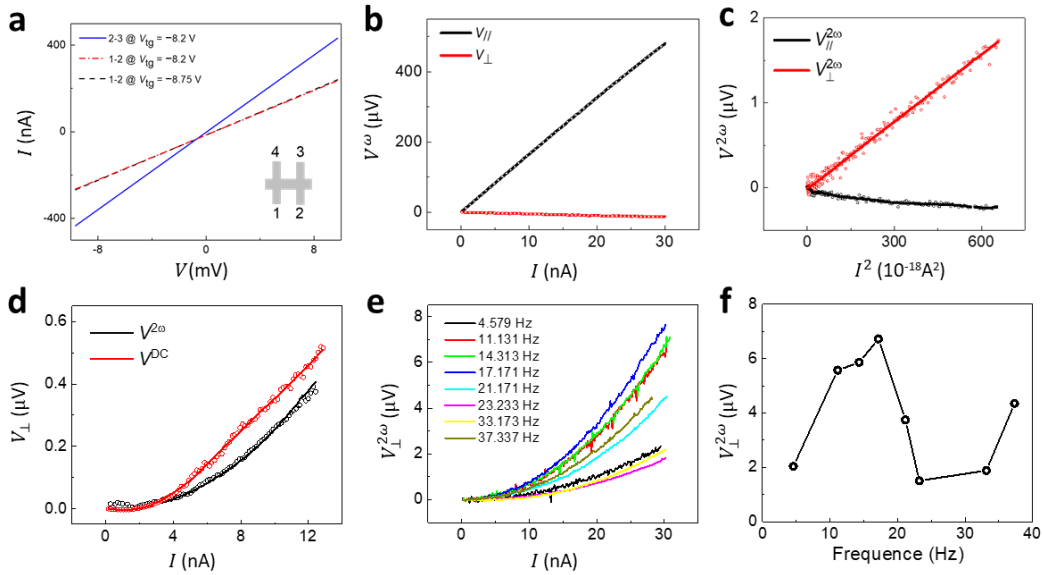
In supplementary Fig. 8, we present the additional nonlinear transport data in our sample A. The second harmonic Hall voltage scales linearly with the square of the injection current. As shown in



supplementary Fig. 8c-8f,  $V_{\perp}^{2\omega}$  measured along different directions change sign near the full filling ( $V_{tg} = -8.7$  V), demonstrating a robust BCD dominated nonlinear Hall effect.

Supplementary Fig. 9 shows the temperature dependence of the nonlinear Hall effect at different fillings. Theoretical calculated Berry curvature dipole as a function of fillings at different temperature is shown in Supplementary Fig. 9a, it matches well with the measured second harmonic Hall voltage (Supplementary Fig. 9b). The temperature dependence at different fillings show a similar behaviour, and the second harmonic Hall voltage decreases when increasing temperature and reduces to nearly zero at  $T = 30$  K. Given the narrow band width of the system (around 10 meV), it is rather suprising that we can still see the nonlinear Hall effect at  $T = 30$  K.

b. Additional transport data in sample B



**Supplementary Fig. 10 | Additional transport data in sample B.** **a.** The two-probe DC  $I$ - $V$  curves for our tWSe<sub>2</sub> sample B at various gate voltages between different contacts. **b.** First harmonic longitudinal and Hall voltage as a function of  $I$ . **c.** Second harmonic longitudinal and Hall voltage as a function of  $I^2$ . **d.** DC component in the nonlinear Hall effect. **e.** Nonlinear Hall voltage as a function of injection current at different frequency. **f.** Frequency dependence of the second harmonic Hall voltage at  $I = 30$  nA.

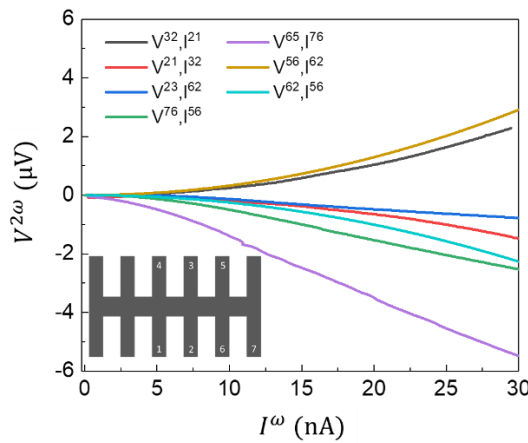
Additional transport data in sample B is shown in Supplementary Fig. 10. We have performed two-probe DC measurements between different contacts we used in the nonlinear Hall measurements. As shown in supplementary Fig. 10a, the linear shape indicates the Ohmic contact in our device and excludes the existence of the diode at the contact/sample interface. Therefore, contact junction induced rectification can be excluded<sup>5</sup>.



The first harmonic voltage response at  $V_{tg} = -8.2$  V is shown in supplementary Fig. 10b. The longitudinal voltage  $V_{//}$  scales linearly with longitudinal current  $I$ . A small transverse voltage  $V_{\perp} \approx 1\%$  of  $V_{//}$  is observed. By correcting the misalignment of the electrodes, nearly zero  $V_{\perp}$  is obtained, suggesting that the device is a non-magnetic system with protected time-reversal symmetry at such a gate voltage. Supplementary Fig. 10c shows the second-harmonic voltage response  $V^{2\omega}$  versus  $I^2$ , we find that the transverse voltage depends linearly on  $I^2$ , while the longitudinal voltage is nearly zero and shows nonlinear dependence. This Hall dominated quadratic  $V - I$  characteristic verifies the BCD induced nonlinear Hall effect in tWSe<sub>2</sub>.

The nonlinear Hall voltage consists of a second harmonic component and a DC component<sup>6</sup>, it can be described as  $V_{\perp} \propto [I_0 \sin(\omega t)]^2 = [I_0^2 + I_0^2 \sin(2\omega t - \pi/2)]/2$ . The DC component of the Hall voltage has been tested and plotted in supplementary Fig. 10d. It shows a similar behaviour with the second harmonic component.

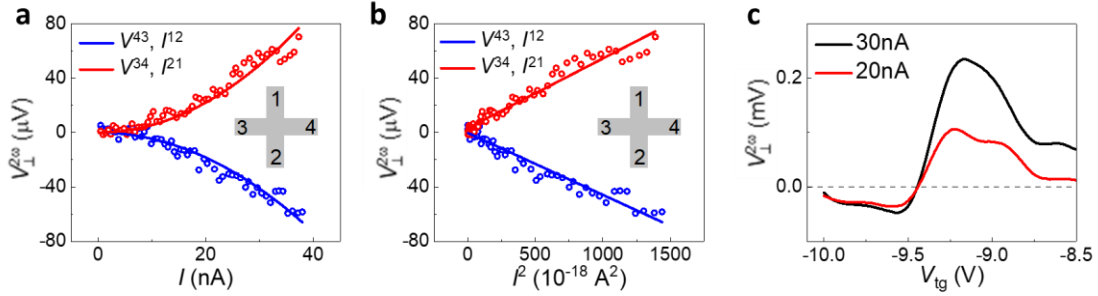
The frequency dependence of the nonlinear Hall signal has been measured and shown in supplementary Fig. 10e and 10f. The nonlinear Hall signal show no significant change with frequency, which is consistent with previous reports<sup>5, 7</sup>. From the working principle, the nonlinear Hall effect has two frequency limiting factors. First, it will breakdown when the frequency is comparable to  $1/\tau$  ( $\tau$  is the scattering time, depending on the charge carrier mobility in the sample), that is around THz. Second, it may not work when the input frequency processes an energy comparable to the flat band width (at the order of tens meV for twisted WSe<sub>2</sub>), which is also in the order of THz. In this study, the measuring frequency has constrictions. Our cryogenic setup installed with a superconductor magnet is not suitable for high-frequency measurement. This is because that the total length of the cables for collecting signals is in the range of 3-4 meters and the conducting Si substrate is used as the back gate for the device for tuning carrier density. All these cause a high parasitic capacitance and thus limit the frequency response. To study systematically the frequency response of the devices, we need to redesign the device structure and the measurement setups.



**Supplementary Fig. 11** | Nonlinear Hall response at different regions of sample B.

For sample B, the second harmonic Hall voltages measured in different sample regions are shown in Supplementary Fig. 11. The inset shows the schematic of the electrode geometry. For example,  $V^{32}, I^{21}$  means that the second harmonic Hall voltage  $V^{32}$  is measured through probes 3 and 2 when current is injected through probes 2 and 1. The data in main text are measured from the middle region with electrodes 1 to 4. In Supplementary Fig. 11, we provide second harmonic Hall voltages measured from two other regions by using electrodes 2 to 6 and electrodes 5 to 7. Qualitatively, the nonlinear Hall effect exists in all sample regions we measured. The quantity is slightly different from region to region because of the twist angle inhomogeneity and strain inhomogeneity.

c. Additional transport data in sample C



**Supplementary Fig. 12 | Other nonlinear transport data in sample C.** **a,b,** Second harmonic Hall voltage measured from different combinations of electrodes as functions of current amplitude and the square of current amplitude at gate voltage  $V_{tg} = -9.6$  V. Dots are measured value and lines are fitted curves. Inset: electrode configuration of the device. The Hall voltage which scales quadratically with inject current demonstrate the nonlinear Hall effect. **c,** Second harmonic Hall voltage at different current amplitude as a function of gate voltage.

In Supplementary Fig. 12, we present the additional nonlinear transport data in our sample C. The second harmonic Hall voltage scales linearly with the square of the injection current. As shown in Supplementary Fig. 12c, both the two curves change sign at  $V_{tg} = -9.44$  V, demonstrating a robust BCD dominated nonlinear Hall effect.

## V. Analysis of the temperature dependent nonlinear Hall effect

Reference 8 has constructed a general scaling law of the nonlinear Hall effect as

$$V_{\perp}^{2w}/(V_{\parallel})^2 \approx A_1 \sigma_{xx0}^{-1} \sigma_{xx}^2 + A_2 \sigma_{xx0}^{-2} \sigma_{xx}^2 + A_3 (\sigma_{xx0}^{-1} \sigma_{xx} - \sigma_{xx0}^{-2} \sigma_{xx}^2) + A_4 \quad (5)$$

where  $\sigma_{xx0}$  is the longitude conductivity in the zero-temperature limit,  $\sigma_{xx}$  is the longitude conductivity, and the scaling parameters can be described as

$$A_1 = C^{sk,2} \quad (6)$$

$$A_2 = C_0^{sj} - C_1^{sj} + C_{00}^{sk,1} - C_{11}^{sk,1} \quad (7)$$

$$A_3 = C_0^{sj} - C_1^{sj} + C_{01}^{sk,1} - 2C_{11}^{sk,1} \quad (8)$$

$$A_4 = C^{in} + C_1^{sj} + C_{11}^{sk,1} \quad (9)$$

where the coefficients stand for the intrinsic ( $C^{in}$ ), side-jump ( $C_i^{sj}$ ), intrinsic skew-scattering ( $C_{ij}^{sk,1}$ ), and extrinsic skew scattering ( $C_{ij}^{sk,2}$ ) contributions with static ( $i = 0$ ) and dynamic ( $i = 1$ ) scattering source<sup>8</sup>. In the low temperature limit, the third term on the right in Eq. (5) can be neglected<sup>9</sup>, resulting in the linear relationship between  $V_{\perp}^{2w}/(V_{\parallel})^2$  and  $\sigma_{xx}^2$ .

$$V_{\perp}^{2w}/(V_{\parallel})^2 \approx A_1 \sigma_{xx0}^{-1} \sigma_{xx}^2 + A_2 \sigma_{xx0}^{-2} \sigma_{xx}^2 + A_4 \quad (10)$$

Our experimental results can be well-fitted by Eq. (10), implying that both intrinsic and extrinsic elements contribute to our observation. To get a quantitative result of the intrinsic contribution using this scaling law, a large number of samples are needed to get their conductivity in the zero-temperature limit. However, a higher nonlinear Hall signal at a lower  $\sigma_{xx}$ , and the sign change behaviour at the full filling of the superlattice, demonstrate that the Berry curvature dipole induced nonlinear Hall effect dominates in our sample.

## VI. Angular dependent nonlinear Hall effect

The non-zero second harmonic Hall signal along all directions comes from the inhomogeneous strain which breaks the rotational and mirror symmetry. In previous reports about WTe<sub>2</sub> where a mirror plane exists, dipole must be pinned by the mirror symmetry. So the nonlinear Hall signal vanishes when the injection current is parallel to the dipole.

But in our case, the three-fold rotational and mirror symmetries are broken. If we use a uniaxial strain model, the angular dependence of the nonlinear Hall response can be expressed by<sup>7, 10</sup>:

$$\frac{V_{\perp}^{2\omega}}{(V_{\parallel}^{\omega})^2} \propto \frac{\rho_{xx}\rho_{yy}(D_x\rho_{xx}\cos\theta + D_y\rho_{yy}\sin\theta)}{(\rho_{xx}\cos^2\theta + \rho_{yy}\sin^2\theta)^2} \quad (11)$$

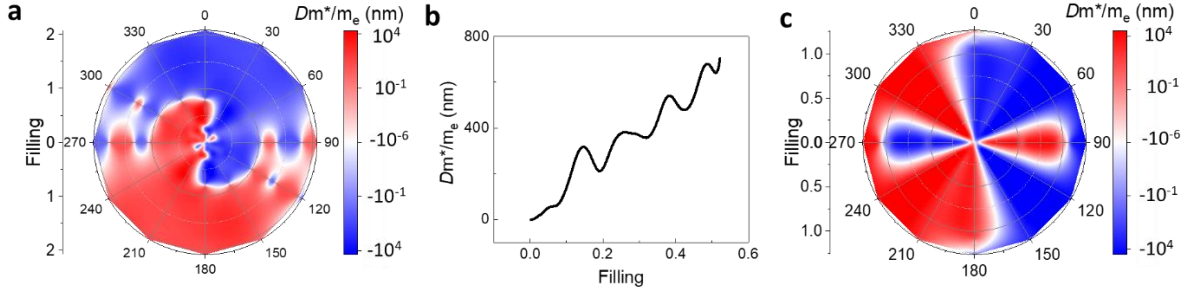
where x (y) is the zigzag (armchair) direction of WSe<sub>2</sub>, and  $\theta$  is the angle between the current injection direction and zigzag direction. So, for a given strain and filling factor, there is a specific current injection direction  $\tan\theta = -\frac{D_x\rho_{xx}}{D_y\rho_{yy}}$ , along this direction, the nonlinear Hall signal vanishes.

As a result, there are some white area with zero nonlinear Hall signal in our mapping.

However, for a given current injection direction, once we tuned the filling, the direction and value of the dipole can change because it is not pinned by mirror symmetry, and then the nonlinear Hall signal can be restored. In this sense, we say that we always have a non-zero nonlinear signal in a certain direction.

## VII. Dipole, responsivity and noise equivalent power

### a. $Dm^*$ in different samples



**Supplementary Fig. 13 |  $Dm^*/m_e$  in different samples.** **a**, The mapping of  $Dm^*/m_e$  as a function of filling factor and angle in sample A (1L+1L). **b**,  $Dm^*/m_e$  in sample B (2L+2L). **c**, The mapping of  $Dm^*/m_e$  as a function of filling factor and angle in sample C (3L+3L).

The mapping of  $Dm^*/m_e$  as a function of filling factor and angle is illustrated in Supplementary Fig. 13. The highly anisotropic value of  $D$  displays similar features with the value of  $V_{\perp}^{2\omega}$ . As shown in this figure, sample B (2L+2L) produces the lowest value, this can be explained by the following reasons. Inversion symmetry is preserved in both pristine bilayer WSe<sub>2</sub> and 0°+θ twisted double-bilayer WSe<sub>2</sub> (sample B). The breaking of the inversion symmetry in sample B is achieved by applying an electric field from the top gate. In sample B, the Berry curvature pocket comes from extrinsic electric field effects. Thus, it is reasonable that the Berry curvature dipole is smaller in this four-layer sample than in monolayer-monolayer twisted and trilayer-trilayer twisted samples which break inversion symmetry even without twisting. In our work, the much higher value of  $\gamma$  in twisted double monolayer/trilayer than that in twisted double bilayer also suggests that the strength of inversion symmetry broken in bilayer induced by  $V_{tg}$  cannot compete with that of intrinsically inversion asymmetric monolayer/trilayer.

### b. Responsivity

The responsivity  $\gamma$  is calculated from  $\gamma = \frac{V_{\perp}^{2\omega}}{I^2 R}$ , where  $V_{\perp}^{2\omega}$  and  $I$  data were taken from lock-in SR830, the resistance  $R$  was obtained by  $R = \frac{V_{\parallel}^{\omega}}{I}$ . For sample B with a Hall bar geometry, the resistance was obtained from a four-probe measurement, the input voltage was taken as the voltage difference between the middle two electrodes. For sample A and sample C with a disk geometry, the resistance was obtained from the Van der Pauw method.

Supplementary Table 7 lists the responsivity and other parameters from our experiment and previous reports when the responsivity has its maximum value. To date, the largest responsivity is  $2.3 \times 10^4$  at room temperature and  $2 \times 10^4$  at low temperature. Taking our data at  $T = 1.5$  K,  $\theta = 0^\circ$ , half filling in sample A, the responsivity we obtained is  $\gamma = 1.2 \times 10^{10}$  V W<sup>-1</sup>, which is six

orders of magnitude higher than the maximum value reported so far. We notice that  $\frac{V_{\perp}^{2\omega}}{I^2}$  and  $\frac{V_{\perp}^{2\omega}}{(V_{\parallel})^2}$  can also characterize the strength of the nonlinear Hall effect. The value of  $\frac{V_{\perp}^{2\omega}}{I^2}$  and  $\frac{V_{\perp}^{2\omega}}{(V_{\parallel})^2}$  in our sample is still larger than the values found in other materials. It can also be foreseen that the artificially constructed van der Waals materials with controlled symmetries would definitely bring us new classes of materials with designed or tailored physical properties that has never been reached. The maximum responsivity in sample B at  $T = 1.5$  K is  $5.1 \times 10^6$  VW<sup>-1</sup>. And the maximum responsivity in sample C at  $T = 1.5$  K is  $3.9 \times 10^7$  VW<sup>-1</sup>.

**Supplementary Table 7 | Responsivity and other parameters compared with previous experiments.**

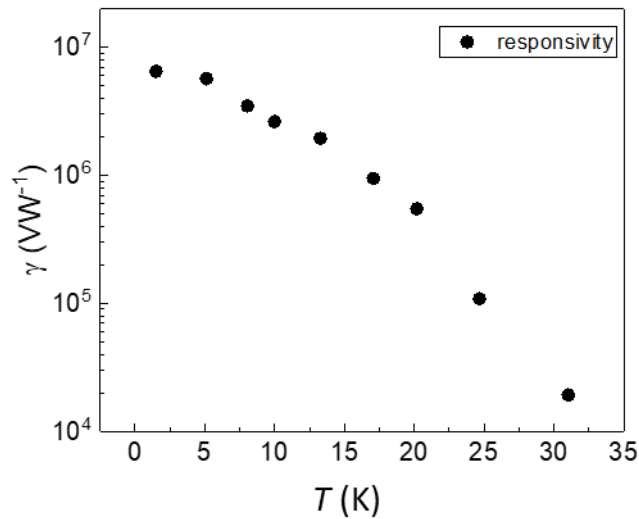
Materials	Mechanism	$\gamma$ (VW <sup>-1</sup> )	$D m^*/m_e$ (nm)	$\frac{V_{\perp}^{2\omega}}{I^2}$ (VA <sup>-2</sup> )	$\frac{V_{\perp}^{2\omega}}{(V_{\parallel})^2}$ (V <sup>-1</sup> )	T (K)	Reference
Sample A	Nonlinear Hall effect	$1.2 \times 10^{10}$	19625	$9.7 \times 10^{17}$	160	1.5	Our work
Sample B	Nonlinear Hall effect	$5.1 \times 10^6$	703	$1.5 \times 10^{10}$	104	1.5	Our work
Sample C	Nonlinear Hall effect	$3.9 \times 10^7$	27046	$1.36 \times 10^{12}$	991	1.5	Our work
Bilayer WTe <sub>2</sub>	Nonlinear Hall effect	$2 \times 10^4$	1.5	$2 \times 10^8$	2	10	[5]
Few-layer WTe <sub>2</sub>	Nonlinear Hall effect	0.19	0.021	7.2	$5 \times 10^{-3}$	1.8	[7]
Graphene	Ballistic rectifier	$2.3 \times 10^4$	-	$5.8 \times 10^6$	92	300	[11]
Graphene	Ballistic rectifier	111	-	$6.1 \times 10^6$	$2 \times 10^{-3}$	300	[12]
Monolayer MoS <sub>2</sub>	B-field induced transport	300	-	$3.6 \times 10^4$	2.5	2	[13]
BiTeBr	B-field induced transport	0.2	-	200	$2 \times 10^{-4}$	2	[14]

Due to the large responsivity achieved at low temperature, a small power input can give a large response, therefore the device is indeed a useful and sensitive detector. For frequency doubling, the device may not show major advantageous compared to mature technology. However, the device based on the nonlinear Hall effect provide a new device structure and mechanism for second harmonic generation. Different from diodes or transistors which can be used to generate distorted double frequency (the output signal needs to be filtered), the frequency doubling/second-order nonlinearity effect is from an intrinsic material property (the symmetry breaking induced Berry curvature dipole). The doubled frequency signal generated is distortionless, and device is suitable for operation at cryogenic temperature range. Such a new effect may address some of the limitation of the existed technologies in future. The device does not have any thermal voltage threshold or

the transition time innate to semiconductor junctions/devices. It may work for ultra-low signals. In principle, the working frequency of the nonlinear Hall effect can reach THz (considering the band width and scattering time in twisted WSe<sub>2</sub>), this can give potential applications in high-frequency second harmonic generation and rectification<sup>15</sup>. Besides that, the device may serve as a detector for probing and measuring the berry curvature dipole amplitude in quantum materials.

#### c. Temperature dependence of the responsivity

Temperature dependent responsivity of sample B is shown in Supplementary Fig. 14. Since the nonlinear Hall signal decreases when increasing the temperature, the responsivity decreases for three orders when the temperature increases from 1.5K to 30K. Given the narrow moiré band width of the system (around 10 meV), it is rather supersizing that we can still see the nonlinear Hall effect at 30 K.

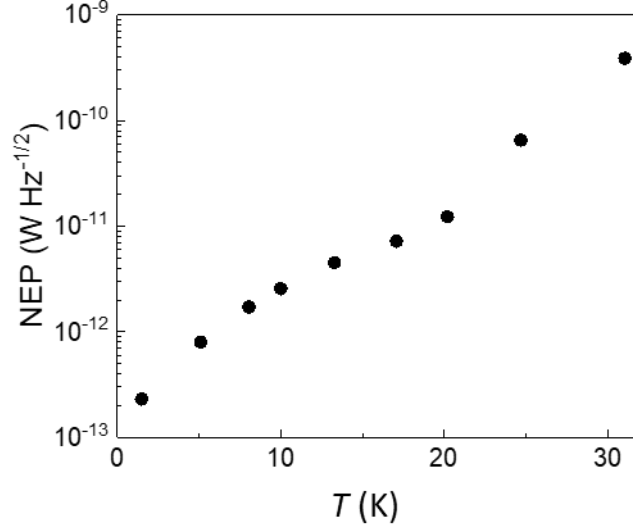


**Supplementary Fig. 14 | Temperature dependent responsivity in sample B at  $V_{tg} = -8.2$  V (corresponding to 0.35 filling).** The uncertainty for the responsivity data is 1%. The error bar plotted in the figure is too short and is covered by the dots.

#### d. Noise equivalent power

As possible detectors, the noise equivalent power is as important as the responsivity. For the low-frequency noise measurement, the output signals were acquired by Keysight InfiniiVision 2000 X-Series Oscilloscope at a sampling rate of  $512 \text{ s}^{-1}$ , a total time 50s was used to measure the noise from 0.04Hz to 512Hz. The noise spectral density is obtained by using the PSD function in MATLAB. The noise equivalent power (NEP) value is then defined as the voltage noise spectral density divided by the responsivity. The temperature-dependent NEP is shown in the Supplementary Fig. 15. Because the responsivity decreases and the thermal noise increases when

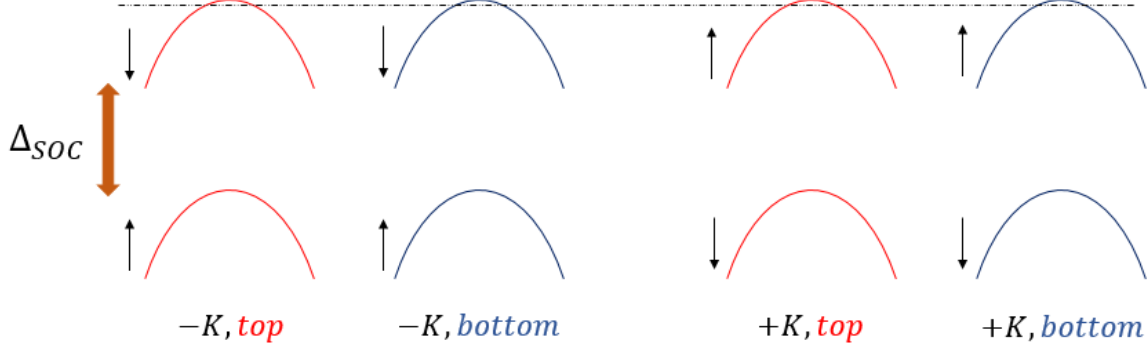
increasing device temperature, according to  $NEP = S/\gamma$ , where  $S$  is the voltage noise spectral density and  $\gamma$  is the responsivity, the NEP increases when increasing temperature. The smallest NEP value obtained at  $T=1.5$  K is  $0.23 \text{ pW Hz}^{-1/2}$ , which is comparable to  $0.64 \text{ pW Hz}^{-1/2}$  for graphene ballistic nano-rectifier<sup>11</sup> and  $1.5 \text{ pW Hz}^{-1/2}$  for Schottky barrier diode<sup>16</sup>. It should be mentioned that our device is not a mature detector, there is a large room for the NEP to be optimized. Meanwhile, our current experimental setup is not designed for ultra-low noise measurement. So, better NEP data from our devices could be obtained by using a dedicated setup for the measurement.



**Supplementary Fig. 15 | Temperature dependent noise equivalent power in sample B.** The uncertainty for the responsivity data is 1%. The error bar plotted in the figure is too short and is covered by the dots.

### VIII. The continuum model

Monolayer and trilayer  $\text{WSe}_2$  are both inversion asymmetric with similar spin polarized valence band edges, while bilayer  $\text{WSe}_2$  is inversion symmetric with spin-degenerated valence band edge. As we only consider the first moiré band, for explicit, to analyze the band structures and the BCD qualitatively using AA stacking twisted bilayer  $\text{WSe}_2$  model is appropriate (see Supplementary Fig. 16 for the band dispersion used in the calculation). Theoretical calculations based on twisted bilayer  $\text{WSe}_2$  have been used in sample A. Below is the detailed information in the calculation<sup>3</sup>:



**Supplementary Fig. 16 | Band dispersion for twisted bilayer WSe<sub>2</sub> in our calculation where inversion symmetry is broken by spin-orbital coupling.** The band for top/bottom layer is labelled in red/blue.

The moiré bands are captured by the continuum Hamiltonian  $H = \sum_{\xi} \int dr \psi_{\xi}^{\dagger}(r) \hat{H}_{\xi}(r) \psi_{\xi}(r)$  with

$$\hat{H}_{\xi}(r) = \begin{pmatrix} \hat{H}_{b,\xi} + \Delta_b(r) & T_{\xi}(r) \\ T_{\xi}^{\dagger}(r) & \hat{H}_{t,\xi} + \Delta_t(r) \end{pmatrix} \quad (12)$$

Here the field operator  $\psi_{\xi}^{\dagger} = (\psi_{b,\xi}^{\dagger}, \psi_{t,\xi}^{\dagger})$ .  $\xi$  is the valley index.  $\hat{H}_{b(t),\xi}$  denotes the layer and valley dependent Hamiltonian and is given by

$$\hat{H}_{l,\xi} = -\frac{\hbar^2}{2m^*} (\hat{k} - K_{\xi,l}^m)^2 - \frac{l\Delta_z}{2} \quad (13)$$

Where  $l = b, t$  labels the bottom(top) layer,  $m^*$  is the effective mass of valence band,  $\Delta_z$  is the staggered layer potential generated by the vertical displacement field.  $\Delta_l(r), T(r)$  represent the intralayer and interlayer moiré potential respectively and are given by

$$\Delta_l(r) = V \sum_{i=1,2,3} e^{i(g_i \cdot r + l\psi)} + h.c. \quad (14)$$

$$T_{\xi}(r) = w(1 + e^{-i\xi g_2 \cdot r} + e^{-i\xi(g_1 + g_2) \cdot r}). \quad (15)$$

Where the moiré reciprocal lattice vectors  $g_i = \frac{4\pi}{\sqrt{3}L_M} \left( \cos \frac{2(i-1)\pi}{3}, \sin \frac{2(i-1)\pi}{3} \right)$ . The model parameters are  $(m^*, \Delta_z, w, V, \psi) = (0.44m_e, 10\text{meV}, 9.7\text{meV}, 15\text{meV}, 91^\circ)^{17}$ .

The strained twisted WSe<sub>2</sub> is modelled by introducing a strain along the  $\varphi$  direction with a strength  $\epsilon$  on the bottom layer. The strain tensor  $\epsilon$  can be written as



$$\boldsymbol{\varepsilon} = \epsilon \begin{pmatrix} \cos^2 \varphi - \nu \sin^2 \varphi & (1 + \nu) \cos \varphi \sin \varphi \\ (1 + \nu) \cos \varphi \sin \varphi & \sin^2 \varphi - \nu \cos^2 \varphi \end{pmatrix} \quad (16)$$

where  $\nu = 0.19$  is the Poisson ratio of WSe<sub>2</sub>. Under this strain, the Dirac point for monolayer TMDC is shifted to  $D_\xi = (I - \varepsilon)K_\xi - \xi A$  with the effective gauge field  $A = \frac{\sqrt{3}}{2a_0} \beta (\epsilon_{xx} - \epsilon_{yy}, -2\epsilon_{xy})$ .  $\beta$  is adopted as 2.30 in our calculation according to previous first principle calculation for strained WSe<sub>2</sub> (Ref. 18). Then the continuum Hamiltonian of this strained WSe<sub>2</sub> can be obtained by simply replacing  $\hat{H}_{b,\xi}$  in Eq. (13) as

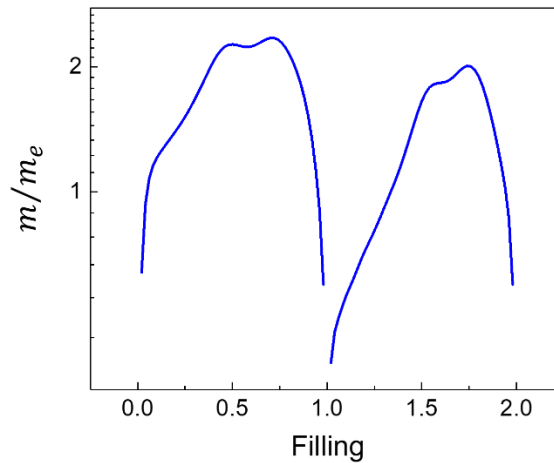
$$\hat{H}_{b,\xi} = -\frac{\hbar^2}{2m^*} (\hat{k} - D_\xi^m)^2 - \frac{\Delta_z}{2} \quad (17)$$

Using the above model, we get the band structures shown in Fig. 4c.

## IX. Effective mass renormalization

### a. Single-particle effective mass

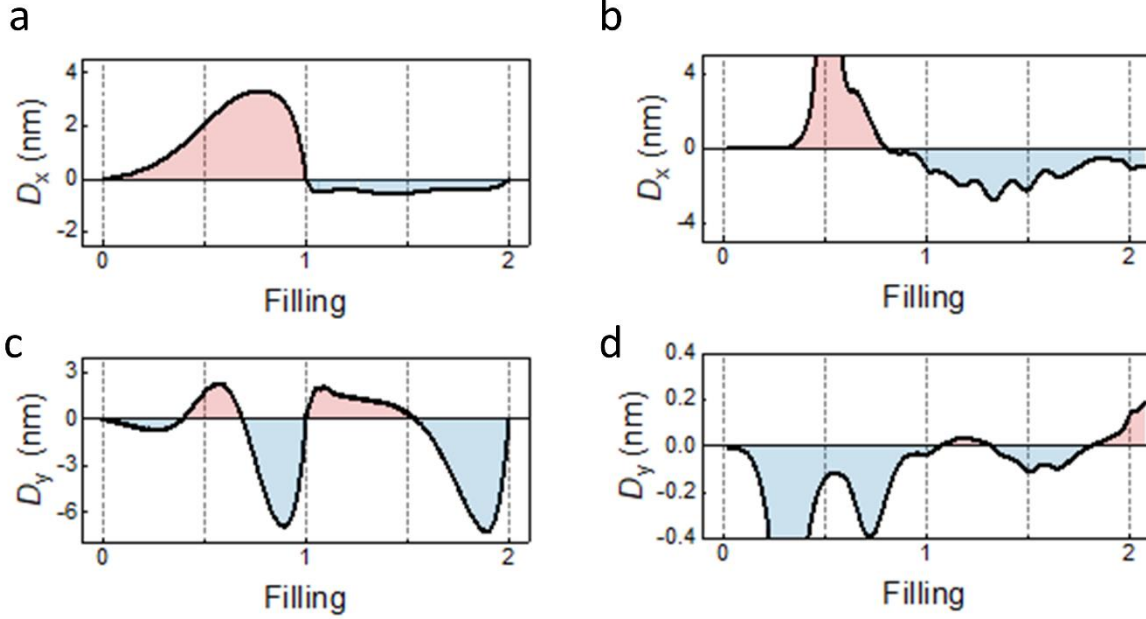
The effective mass as a function of filling can be calculated using the expression:  $m = \frac{2\pi\hbar^2 D(E)}{g_{sv}} = \pi\hbar^2 D(E)$  where  $\hbar$  is the reduced Planck constant,  $g_{sv} = 2$  is the spin(valley) degeneracy and  $D(E)$  is the moiré density of states. The single-particle effective mass can be computed as shown in Supplementary Fig. 17.



**Supplementary Fig. 17 | Calculated single-particle effective mass.**

### b. Effective mass renormalization in the moiré band

In a recent theoretical study, Das Sarma et al found that the  $1/N$  expansion, rather than the 1-loop perturbative renormalization group, can quantitatively explain the large effective mass (25 times larger than that in monolayer graphene) near the charge neutrality of twisted bilayer graphene<sup>19</sup>. Considering similar effective mass renormalization effects in our samples, we found that away from the half-filling, the data can be fitted roughly using  $m^* = \alpha\pi\hbar^2 D(E)$ , where  $\alpha = 40$  is the renormalization parameter (as shown in Supplementary Fig. 18).



**Supplementary Fig. 18 | Berry curvature dipole fit using  $m^* = \alpha\pi\hbar^2 D(E)$ .** **a, c**, Computed Berry curvature dipole  $D$  as a function of filling.  $D_x$  (**a**) and  $D_y$  (**c**) are the dipole along the zigzag and armchair directions respectively. **b, d**, Experiment estimated  $D$  in sample A at (**b**)  $\theta = 0^\circ$  and (**d**)  $\theta = 90^\circ$  as a function of the filling factor.

### c. Effective mass singularity near the half-filling

At the half-filling, the electron-electron interaction can induce a metal to correlated insulator transition which could make the effective mass divergent. The on-site Coulomb energy  $U$  of each site is estimated to be  $e^2/(4\pi\epsilon d_0)$ , where  $e$  is the elementary charge,  $\epsilon$  is the effective in-plane dielectric constant<sup>20</sup> including screening and  $d_0$  is the effective distance between each site. Considering  $d_0$  is 40% of the moiré wavelength and  $\epsilon = 3\epsilon_0$ , we get  $U = e^2\theta/(4\pi\epsilon_0 a\kappa)$ , where  $\kappa = 0.4 \times 3 = 1.2$  and  $a = 0.33$  nm is the WSe<sub>2</sub> lattice constant. For  $\theta = 2^\circ$ ,  $U = 10.5$  meV, which is comparable to the moiré band width  $W_b$ . A large ratio for  $U/W_b$  suggests the possibility of a Mott-like insulator phase at half-filling of the band. The formation of a Mott-like insulator driven by Coulomb interactions between electrons is quite possible.

According to previous studies<sup>21, 22, 23</sup>, the Mott transition in the Hubbard model is driven by the effective mass singularity  $m^*/m \propto [1 - (U/U_c)^2]^{-1} \rightarrow \infty$  when the interaction energy  $U$  approaches

the critical energy  $U_c \approx W_b$ , where  $m$  is the non-renormalized effective mass. Compared with traditional materials such as  $\text{Sr}_{1-x}\text{La}_x\text{TiO}_3$  (Ref. 24), the effective mass divergence is more likely to take place in the moiré band in  $\text{tWSe}_2$  with ultra-small band width. When the Fermi level is tuned close to the half-filling, the system undergoes a metal to correlated insulator transition, resulting in a sharp increase of the nonlinear Hall response.

## X. Interaction induced gapped phase at the half filling

The nonlinear Hall signal of  $\text{tWSe}_2$  sample has a peak at half-filling (Fig.3d in main text) when the resistance has a peak at half filling (Fig.1g in main text). The emergence of a peak in resistivity at half-filling is a strong indication that the system is near an interaction driven correlated phase. It is important to note that we further measured the temperature dependence of the resistance near half-filling and away from half-filling for the twisted double bilayer sample (as shown in Supplementary Fig.7). As temperature decreases, the resistance increases near half-filling (at 0.51 filling). At 0.46 filling, for example, the resistance decreases as temperature decreases. This gives strong evidence that near half-filling, we may have observed an interaction driven correlated phases and we need to use a different theory to describe the nonlinear Hall effect near half-filling.

We took into account the interaction effect and performed a mean-field calculation for the system at half-filling. As first proposed in the study for twisted bilayer graphene, there are two possible gapped phases which are the valley-polarized phase (VP) and the inter-valley coherent state (IVC) respectively<sup>25</sup>. Both of these phases cause an energy gap at the Fermi energy which explains the insulating behaviour of our twisted bilayer  $\text{WSe}_2$  samples. However, we show below that the IVC has lower energy than the VP phase. Also, the VP phase breaks time-reversal symmetry spontaneously which does not match our experimental findings. Below are the details of the calculation:

We present a mean-field treatment to illustrate the ordered states in  $\text{tWSe}_2$ , with the following simplified Hamiltonian on the top valence bands (with two valleys):

$$H = H_0 + H_V = \sum_{\xi, k} E_{\xi}(k) c_{\xi}^{\dagger}(k) c_{\xi}(k) + \frac{V_0}{2N} \sum_{k_1 k_2 q} c_{\xi}^{\dagger}(k_1 + q) c_{\xi}^{\dagger}(k_2 - q) c_{\xi}(k_2) c_{\xi}(k_1) \quad (18)$$

The first term is the single particle kinetic energy and the second is the interaction term. Within Hartree-Fock approximation, the Hartree term can be safely dropped, which is expected to be cancelled by some charge background. The remaining Fock exchange term can lead to symmetry broken states:

$$\Sigma_F = -\frac{V_0}{N} \sum_{kk'} \langle c_{\xi}^{\dagger}(k') c_{\xi'}(k') \rangle c_{\xi}^{\dagger}(k) c_{\xi}(k) \quad (19)$$

The resulting mean field Hamiltonian is written by  $H_{MF} = H_0 + \Sigma_F$ . We would like to compare the energies of valley polarized state and intervalley-coherent state.

### 1) Valley polarized state (VP)

In this state, we assume

$$\frac{1}{N} \langle c_{\xi}^{\dagger}(k) c_{\xi'}(k) \rangle = \frac{1}{2} \delta_{\xi\xi'} + \phi_1 \sigma_{\xi\xi}^z. \quad (20)$$

With  $\phi_1$  is the order parameter which can be determined self-consistently. In the fully gapped phase,  $\phi_1 = \frac{1}{2}$ .

## 2) Intervalley coherent state (IVC)

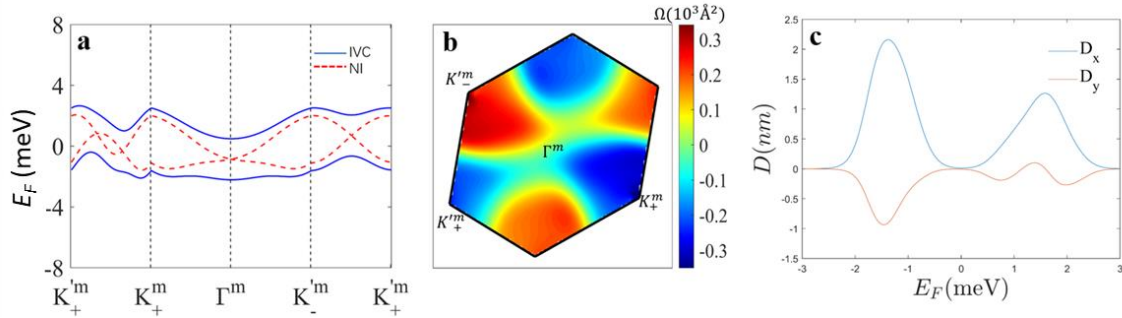
In this state, we assume

$$\frac{1}{N} \langle c_{\xi}^{\dagger}(k) c_{\xi'}(k) \rangle = \frac{1}{2} \delta_{\xi\xi'} + \phi_2 \sigma_{\xi\xi}^x \quad (21)$$

where  $\phi_2$  is the order parameter which can be determined self-consistently. In the fully gapped phase,  $\phi_2 \rightarrow \frac{1}{2}$ . By comparing the total energy, we find:

$$E_{IVC} - E_{VP} = -\frac{1}{V_0} \sum_k (E_+(k) - E_-(k))^2 \quad (22)$$

That means the IVC state is energetically more favourable than the VP state. Also the VP state breaks the time-reversal symmetry, which does not conform to the observation of the nonlinear Hall signal. Based on the two reasons, we consider the IVC state to be the ground state at the half-filling.



**Supplementary Fig.19** | **a**, The band structure of the non-interacting phase (NI) and the reconstructed band structure of the IVC phase respectively. It is clear that in the IVC phase, a band gap is induced by interaction. **b**, Berry curvature for the upper band in the IVC state. It is clear that the Berry curvature is sizable in the reconstructed band structure. **c**, Berry curvature dipole of the IVC phase at different energy. We set the interaction strength  $V_0 = 0.8 W$  ( $W$  is the bandwidth). The two peaks come from the split Fermi surface. The Fermi level  $E_F$  scans from band bottom to band top of the two bands in the IVC state.

Even though the IVC phase is supposed to be insulating at half-filling, the sample is highly non-uniform and we expect that, experimentally, it is not possible to tune the sample to half-filling for the whole macroscopic sample, therefore, our sample is still weakly conducting and which allows us to measure the nonlinear Hall response.

Moreover, the IVC phase is insulating only at half-filling. Slightly away from half-filling, the system can be described by the reconstructed bands as the IVC phase is a commensurate insulating phase. As a result, we have also calculated the Berry curvature dipole in the IVC phase using the

reconstructed band structure including the mean-field interaction terms (as shown in Supplementary Fig. 19a). As explained above, the nonlinear Hall response can be written as  $\frac{V_L^{2\omega}}{I^2 R} \propto D \frac{m}{n} R \propto D m R^2$  which has a quadratic dependence on resistance. The interaction induced IVC state may have two effects. First, it enhances the sample resistance which could give rise to a large nonlinear Hall response at half-filling. Second, it could induce a metal to correlated insulator transition which might make the effective mass divergent at half-filling as shown in Supplementary Section IX. Together with the sizable Berry curvature dipole (Supplementary Fig. 19b and c), the responsivity is largely enhanced.

## XI. Comparison between twisted WSe<sub>2</sub> and monolayer WSe<sub>2</sub>

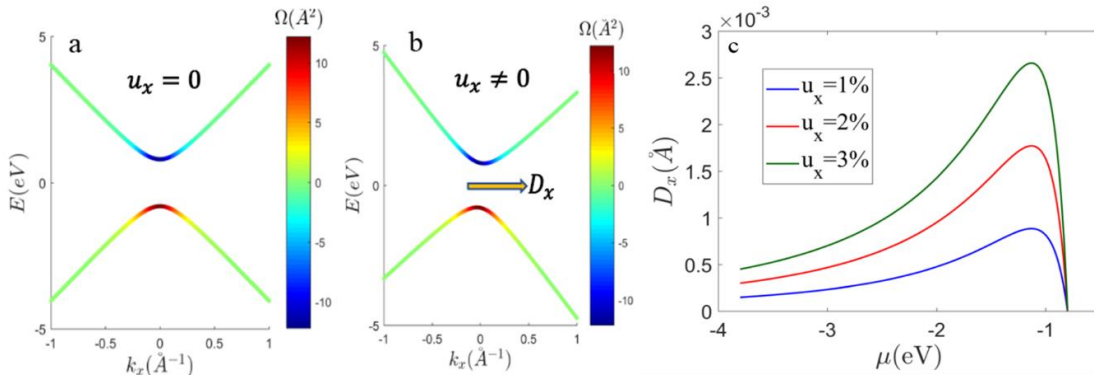
Regarding to a monolayer WSe<sub>2</sub>, to make a comparison, we first show the theoretical calculation of the nonlinear Hall response in monolayer WSe<sub>2</sub> under uniaxial strain. Here we adopt a low energy effective model near K pocket<sup>26</sup>:

$$H = at(\xi k'_x \sigma_x + k_y \sigma_y) + \frac{\Delta}{2} \sigma_z + \xi \gamma a t u_x k'_x \sigma_0 \quad (23)$$

The parameters are set with  $a = 0.332 \text{ nm}$ ,  $t = 1.19 \text{ eV}$ ,  $\Delta = 1.6 \text{ eV}$ ,  $\gamma \approx 0.3$ .  $\xi = \pm 1$  denotes the  $K(K')$  valley.  $k'_x = k_x - \xi A$  with the effective gauge field  $A$ . We assume that the strain is along  $x$  direction, with  $u_x$  characterize the strain strength. The berry curvature for the upper(conduction) and lower(valence) bands reads:

$$\Omega = \mp \frac{\xi \Delta (at)^2}{4 \left( a^2 t^2 k^2 + \frac{\Delta^2}{4} \right)^{\frac{3}{2}}} \quad (24)$$

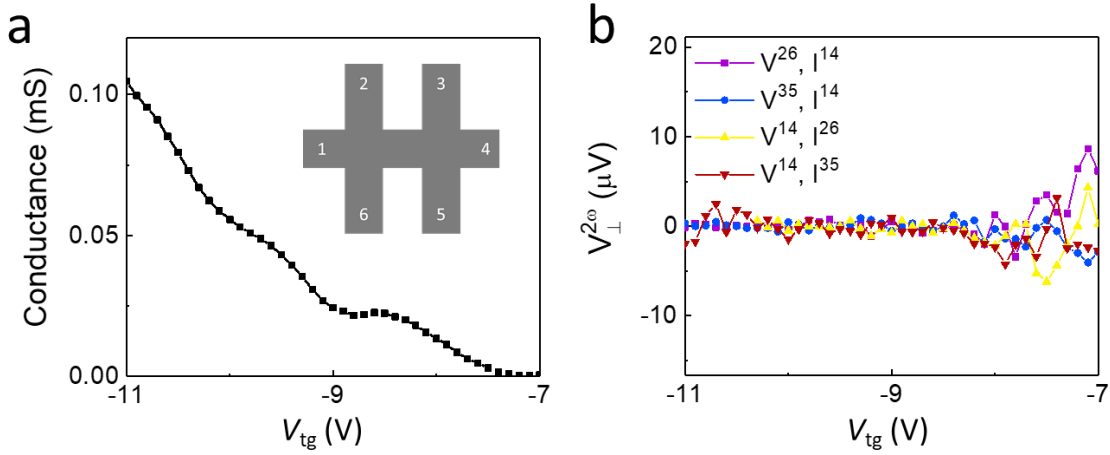
We depict the Berry curvature dipole for strained monolayer WSe<sub>2</sub> under different strain strength in Supplementary Fig. 20c. The order of Berry dipole is  $10^{-3} \text{ \AA}$ , which three orders of magnitude smaller than tWSe<sub>2</sub>. This can be understood by: (1) the local Berry curvature from the remote conduction band near the valence band maxima is small (only  $10 \text{ \AA}^2$ ). (2) The effective mass is much smaller than moiré systems which possess flat bands, leading to a relative lower density of states on Fermi surface.



**Supplementary Fig. 20 | Berry curvature dipole in strained monolayer WSe<sub>2</sub>.** a,b, band dispersion for WSe<sub>2</sub> without (a) and with (b) strain. Under strain along  $x$  direction, a nonzero

Berry dipole  $D_x$  is created. **c**, Calculated Berry dipole for different  $u_x$ . The chemical potential only scans the valence band.

Experimentally, we fabricated monolayer WSe<sub>2</sub> device to examine the nonlinear Hall effect. The results are shown in Supplementary Fig. 21 which indicate only a very small nonlinear Hall signal. Near the threshold voltage (valence band edge), the maximum nonlinear Hall signal is around 10  $\mu$ V, which is three orders smaller than the signal in twisted 1L+1L WSe<sub>2</sub>. Away from the threshold voltage, the nonlinear Hall signal almost vanishes. The maximum dipole calculated in monolayer WSe<sub>2</sub> is 0.05 nm, which is 2-3 orders smaller than that in twisted WSe<sub>2</sub>.



**Supplementary Fig. 21 | Nonlinear Hall effect in monolayer WSe<sub>2</sub>.** **a**, The conductance versus gate voltages at  $T = 1.5$  K. Inset: Schematics of the electrodes. **b**, Second harmonic Hall voltage  $V^{AB}$  measured through probes A and B as functions of current amplitude  $I^{CD}$  (through probes C and D) in different samples.

## XII. Origin of the symmetry breaking.

In this section, the origin of the rotational and mirror symmetry breaking is analyzed. The symmetry breaking can be resulting from spontaneous symmetry breaking due to electron-electron interactions, substrate induced strain or twist angle variation.

First, if there exists only the twist angle variation, the generated nonlinear Hall signal should be very small because the three-fold rotational symmetry is locally reserved. In this case, the twist angle variation only plays a minor role in modifying the nonlinear Hall signals.

The substrate/interface-induced strain in lattice dominates the symmetry breaking effect because the nonlinear Hall effect can be observed when the sample is away from half-filling (in this case interaction effects are not important). We also observed strong nonlinear Hall effect in all of our samples with twist angles ranging from  $2^\circ$  -  $4.5^\circ$ . The symmetry breaking phases are believed to be more delicate and appear only in a small parameter regime.

Electron-electron interactions may induce symmetry breaking phases, such as the nematic phase as in twisted bilayer graphene<sup>1</sup>. However, the two-fold symmetry of the nematic phase will also force the nonlinear Hall effect to be zero. Importantly, our STM images clearly show that there is no remaining two-fold rotational symmetry associated with nematic phase. This further supports the claim that the symmetry breaking is not due to spontaneous symmetry breaking of the electronic state. As we discussed in the main text, the interaction effects are still important as it normalizes the effective mass of the carriers and enhance the nonlinear Hall response.

In summary, the rotational symmetry breaking effects in our devices are mainly caused by the substrate effects. While the interaction induced effective mass renormalization and the twist angle variation play a non-negligible role in modifying the nonlinear Hall response.

### XIII. Calculation of the displacement electric field

According to reference 27, the displacement electric field in bilayer MoS<sub>2</sub> can be calculated roughly by  $U = -\frac{C_g}{C_Q} V_{tg}$ , where  $C_g$  is the top gate capacitance and  $C_Q = \frac{2e^2 m^*}{\pi \hbar^2} = 5.9 \times 10^{-5} \text{ F cm}^{-2}$  is the quantum capacitance of monolayer WSe<sub>2</sub>.

In sample A (twisted double-monolayer WSe<sub>2</sub>):  $V_{tg}$  ranges from  $-7.5 \text{ V}$  to  $-10 \text{ V}$ ,  $C_g = 3.45 \times 10^{-7} \text{ F cm}^{-2}$ . The calculated displacement electric field is  $44 \sim 58 \text{ mV}$  between the top layer and bottom layer.

In sample B (twisted double-bilayer WSe<sub>2</sub>):  $V_{tg}$  ranges from  $-5.82 \text{ V}$  to  $-10 \text{ V}$ ,  $C_g = 1.46 \times 10^{-7} \text{ F cm}^{-2}$ . The calculated displacement electric field is  $14 \sim 24 \text{ mV}$  between the top layer and bottom layer and  $4.6 \sim 8 \text{ mV}$  between adjacent two layers, if we assume that  $U$  is uniformly distributed in the whole sample. This value is similar to that in previous reports<sup>27, 28</sup>, in which the inversion symmetry in bilayer were broken by the electric displacement field ( $U = 7.2 \text{ mV}$  in reference 27). Thus, the inversion symmetry in sample B is broken and the BC hotspot is generated.

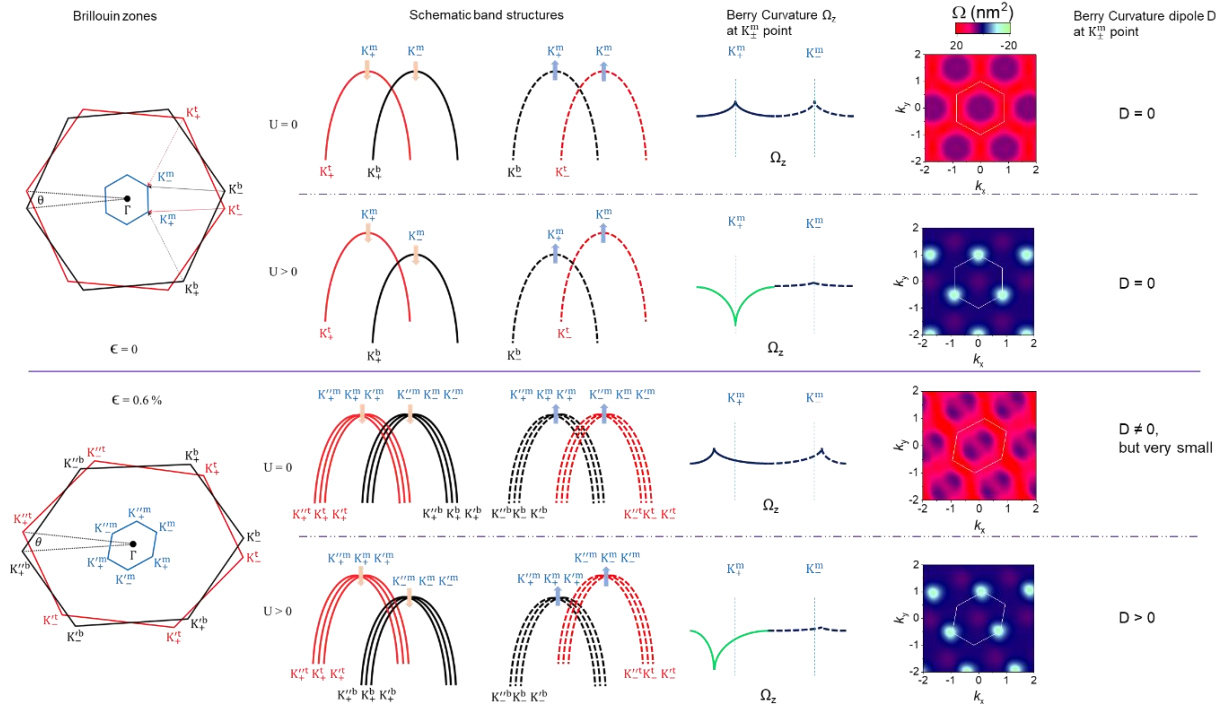
In sample C (twisted double-trilayer WSe<sub>2</sub>):  $V_{tg}$  ranges from  $-7.32 \text{ V}$  to  $-10 \text{ V}$ ,  $C_g = 1.92 \times 10^{-7} \text{ F cm}^{-2}$ . The calculated displacement electric field is  $24 \sim 32 \text{ mV}$  between the top layer and bottom layer and  $4.8 \sim 6.4 \text{ mV}$  between adjacent two layers, if we assume that  $U$  is uniformly distributed in the whole sample.

In the computational modelling, the fitting parameter  $U$  is  $10 \text{ meV}$ , which is relatively smaller than the estimation in sample A. The possible reason is that the strength of the displacement electric field in real samples can be much complicated: (1) the effective mass in pristine monolayer WSe<sub>2</sub> and in twisted WSe<sub>2</sub> samples are different; (2) the interlayer interaction strength in twisted bilayers and pristine bilayers should be different; (3) the interlayer interaction strength in the twist interface is not uniform because there are AA, AB and BA stacking regions; (4) local defects or variance of strains strength can also tune the interlayer interaction strength.

In addition, although sample B and C share similar strength of  $U$ , the values of  $D m^*/m_e$  in the two samples are much different ( $703 \text{ nm}$  for sample B and  $27046 \text{ nm}$  for sample C, as listed in Supplementary table. 7). This difference implies that the strength of inversion symmetry breaking

is different since pristine trilayer/bilayer WSe<sub>2</sub> is inversion asymmetric/symmetric. It also tells us that the inversion symmetry in bilayer WSe<sub>2</sub> can be broken through applied displacement electric field and the BC hotspot can be generated, so that the nonlinear Hall signal can be observed in sample B. The observation of nonlinear Hall effects in tWSe<sub>2</sub> constructed from both inversion symmetric bilayer and inversion asymmetric monolayer/trilayer WSe<sub>2</sub> demonstrate the robustness of the symmetry breaking effects in real tWSe<sub>2</sub> devices.

#### XIV. The effects of strain and displacement electric field on BCD



**Supplementary Fig. 22 | Strain and displacement electric field effect.**

Both the strain and electric field are vital in generating large BCD. Due to the spin-split valence bands in monolayer WSe<sub>2</sub>, the degeneracy of each moiré band is one.

1.  $\epsilon = 0, U = 0$ :  $\Omega_z$  is small,  $D = 0$  (three-fold symmetry forces the dipole to vanish)
2.  $\epsilon = 0, U > 0$ :  $\Omega_z$  is large,  $D = 0$  (three-fold symmetry forces the dipole to vanish)
3.  $\epsilon = 0.6\%, U = 0$ :  $\Omega_z$  is small,  $D \neq 0$  (the BC hotspot is small, so dipole is small)
4.  $\epsilon = 0.6\%, U > 0$ :  $\Omega_z$  is large,  $D > 0$  (the BC hotspot is large, so dipole is large)



## References

1. Kerelsky A, McGilly LJ, Kennes DM, Xian L, Yankowitz M, Chen S, *et al.* Maximized electron interactions at the magic angle in twisted bilayer graphene. *Nature* **572**, 95-100 (2019).
2. Zhang R, Koutsos V, Cheung R. Elastic properties of suspended multilayer WSe<sub>2</sub>. *Appl. Phys. Lett.* **108**, 042104 (2016).
3. Hu J-X, Zhang C-P, Xie Y-M, Law KT. Nonlinear Hall Effects in Strained Twisted Bilayer WSe<sub>2</sub>. Preprint at <https://arxiv.org/abs/2004.14140> (2020).
4. Cao Y, Fatemi V, Fang S, Watanabe K, Taniguchi T, Kaxiras E, *et al.* Unconventional superconductivity in magic-angle graphene superlattices. *Nature* **556**, 43-50 (2018).
5. Ma Q, Xu SY, Shen H, MacNeill D, Fatemi V, Chang TR, *et al.* Observation of the nonlinear Hall effect under time-reversal-symmetric conditions. *Nature* **565**, 337-342 (2019).
6. Sodemann I, Fu L. Quantum Nonlinear Hall Effect Induced by Berry Curvature Dipole in Time-Reversal Invariant Materials. *Phys. Rev. Lett.* **115**, 216806 (2015).
7. Kang K, Li T, Sohn E, Shan J, Mak KF. Nonlinear anomalous Hall effect in few-layer WTe<sub>2</sub>. *Nat. Mater.* **18**, 324-328 (2019).
8. Du ZZ, Wang CM, Li S, Lu HZ, Xie XC. Disorder-induced nonlinear Hall effect with time-reversal symmetry. *Nat. Commun.* **10**, 3047 (2019).
9. Tian Y, Ye L, Jin X. Proper Scaling of the Anomalous Hall Effect. *Phys. Rev. Lett.* **103**, 087206 (2009).
10. Du ZZ, Wang CM, Lu HZ, Xie XC. Band Signatures for Strong Nonlinear Hall Effect in Bilayer WTe<sub>2</sub>. *Phys. Rev. Lett.* **121**, 266601 (2018).
11. Auton G, Zhang J, Kumar RK, Wang H, Zhang X, Wang Q, *et al.* Graphene ballistic nano-rectifier with very high responsivity. *Nat. Commun.* **7**, 11670 (2016).
12. Singh AK, Auton G, Hill E, Song A. Graphene based ballistic rectifiers. *Carbon* **84**, 124-129 (2015).
13. Wakatsuki R, Saito Y, Hoshino S, Itahashi YM, Ideue T, Ezawa M, *et al.* Nonreciprocal charge transport in noncentrosymmetric superconductors. *Sci. Adv.* **3**, e1602390 (2017).
14. Ideue T, Hamamoto K, Koshikawa S, Ezawa M, Shimizu S, Kaneko Y, *et al.* Bulk rectification effect in a polar semiconductor. *Nat. Phys.* **13**, 578-583 (2017).
15. Isobe H, Xu S-Y, Fu L. High-frequency rectification via chiral Bloch electrons. *Sci. Adv.* **6**, eaay2497 (2020).
16. Hesler JL, Crowe TW. NEP and responsivity of THz zero-bias Schottky diode detectors. *2007 Joint 32nd International Conference on Infrared and Millimeter Waves and the 15th International Conference on Terahertz Electronics. IEEE*, 844-845 (2007).
17. Wu F, Lovorn T, Tutuc E, Martin I, MacDonald AH. Topological Insulators in Twisted Transition Metal Dichalcogenide Homobilayers. *Phys. Rev. Lett.* **122**, 086402 (2019).
18. Fang S, Carr S, Casalilla MA, Kaxiras E. Electronic structure theory of strained two-dimensional materials with hexagonal symmetry. *Phys. Rev. B.* **98**, 075106 (2018).
19. Sarma SD, Wu F. Electron-phonon and electron-electron interaction effects in twisted bilayer graphene. *Ann. Phys.* 168193 (2020).
20. Naik MH, Jain M. Ultraflatbands and Shear Solitons in Moiré Patterns of Twisted Bilayer Transition Metal Dichalcogenides. *Phys. Rev. Lett.* **121**, 266401 (2018).
21. Brinkman WF, Rice TM. Application of Gutzwiller's Variational Method to the Metal-Insulator Transition. *Phys. Rev. B.* **2**, 4302-4304 (1970).
22. Furukawa N, Imada M. Mass Anomaly in the Hubbard Model Near Half-Filling. *Correlation Effects in Low-Dimensional Electron Systems*. 210-214 (Springer, 1994).
23. Zhang XY, Rozenberg MJ, Kotliar G. Mott transition in the  $d=\infty$  Hubbard model at zero temperature. *Phys. Rev. Lett.* **70**, 1666-1669 (1993).

- 24. Tokura Y, Taguchi Y, Okada Y, Fujishima Y, Arima T, Kumagai K, *et al.* Filling dependence of electronic properties on the verge of metal-Mott-insulator transition in  $\text{Sr}_{1-x}\text{La}_x\text{TiO}_3$ . *Phys. Rev. Lett.* **70**, 2126-2129 (1993).
- 25. Po HC, Zou L, Vishwanath A, Senthil T. Origin of Mott Insulating Behavior and Superconductivity in Twisted Bilayer Graphene. *Phys. Rev. X.* **8**, 031089 (2018).
- 26. Yu X-Q, Zhu Z-G, You J-S, Low T, Su G. Topological nonlinear anomalous Nernst effect in strained transition metal dichalcogenides. *Phys. Rev. B.* **99**, 201410 (2019).
- 27. Lee J, Mak KF, Shan J. Electrical control of the valley Hall effect in bilayer  $\text{MoS}_2$  transistors. *Nat. Nanotechnol.* **11**, 421-425 (2016).
- 28. Wu S, Ross JS, Liu G-B, Aivazian G, Jones A, Fei Z, *et al.* Electrical tuning of valley magnetic moment through symmetry control in bilayer  $\text{MoS}_2$ . *Nat. Phys.* **9**, 149-153 (2013).